DOES FLUX ALREADY KNOW HOW TO PERFORM PHYSICALLY PLAUSIBLE IMAGE COMPOSITION?

Anonymous authors
Paper under double-blind review

Figure 1: Showcase of our training-free image composition method, **SHINE**. This gallery highlights SHINE's ability to seamlessly integrate subjects into complex scenes, including **low-light conditions, intricate shadows, and water reflections.**

ABSTRACT

Image composition aims to seamlessly insert a user-specified object into a new scene, but existing models struggle with complex lighting (e.g., accurate shadows, water reflections) and diverse, high-resolution inputs. Modern text-to-image diffusion models (e.g., SD3.5, FLUX) already encode essential physical and resolution priors, yet lack a framework to unleash them without resorting to latent inversion, which often locks object poses into contextually inappropriate orientations, or brittle attention surgery. We propose **SHINE**, a training-free framework for **S**eamless, **H**igh-fidelity **I**nsertion with **N**eutralized **E**rrors. SHINE introduces manifold-steered anchor loss, leveraging pretrained customization adapters (e.g., IP-Adapter) to guide latents for faithful subject representation while preserving background integrity. Degradation-suppression guidance and adaptive background blending are proposed to further eliminate low-quality outputs and visible seams. To address the lack of rigorous benchmarks, we introduce *ComplexCompo*, featuring diverse resolutions and challenging conditions such as low lighting, strong illumination, intricate shadows, and reflective surfaces. Experiments on ComplexCompo and DreamEditBench show state-of-the-art performance on standard metrics (e.g., DINOv2) and human-aligned scores (e.g., DreamSim, ImageReward, VisionReward). Code and benchmark will be publicly available upon publication.

1 INTRODUCTION

Image composition, which places a user–specified object into a new scene, is a demanding image editing task. Despite the breathtaking progress of multimodal foundation models (e.g., GPT-5 (OpenAI, 2025), Gemini-2.5 (Gemini2.5, 2025), SeedEdit/Doubao (Shi et al., 2024b), and Grok-4 (gro, 2025)), these generic models still struggle with image composition. Typical failures include imprecise object placement, inconsistent lighting, and the subject's identity drift (see Fig. 2). These limitations indicate that, as of now, massive multimodal pre-training alone has not yet endowed them with sufficient compositional ability for this task. A natural response has been to train specialized models. Yet building large-scale, high-quality, multi-resolution triplet datasets (object, scene, composite) is prohibitively costly. As a result, most composition models are fine-tuned from base models (e.g., FLUX.1-dev (Black Forest Labs, 2024a), FLUX.1-Fill (Black Forest Labs, 2024c), SDXL (Podell et al., 2024)) on synthetic data generated via inpainting or augmentations (Chen et al., 2024c; Yang et al., 2023; Song et al., 2023; Wang et al., 2025a; He et al., 2024).

These models, however, face two main limitations (see Fig. 6): **(i) Lighting realism.** They struggle to achieve natural composition under complex lighting conditions, such as accurate shadow generation or water reflections for the inserted subject. **(ii) Resolution rigidity.** They are tied to a fixed resolution, necessitating downsampling or cropping when applied to varied, high-resolution background images, which degrades generation quality. Notably, such issues are absent in the base models, implying that the underlying physical priors are present but are not effectively exploited by fine-tuned variants. The degradation largely stems from low-quality synthetic datasets, which inherit flaws from inpainting models that often mis-handle shadows and reflections, producing implausible edits, hallucinated content, or incomplete object removal (Yu et al., 2025b; Winter et al., 2025).

There have been prior **training-free** attempts to exploit the priors of text-to-image (T2I) models for advancing image composition, but they fall short for two main reasons. **(i) Inversion bottlenecks.** Most methods (Lu et al., 2023d; Pham et al., 2024; Yan et al., 2025; Li et al., 2024b) depend on accurate image inversion (Song et al., 2021; Lu et al., 2022; Mokady et al., 2023). In practice, inversion constrains the inserted object to the pose of its reference image, often resulting in contextually inappropriate orientations. Moreover, inversion is less effective for classifier-free guidance (CFG) distilled models (e.g., FLUX), where elevated inversion errors degrade identity preservation. **(ii) Fragile attention surgery.** Many training-free approaches rely on attention manipulation (Lu et al., 2023d; Yan et al., 2025; Li et al., 2024b). While compatible with the joint self-attention in Multimodal Diffusion Transformers (MMDiT) (Peebles & Xie, 2023), these methods inherit the instability and hyperparameter sensitivity (Lu et al., 2023d), limiting their robustness.

To bridge these gaps we present **SHINE**, a training-free framework for **S**eamless, **H**igh-fidelity **I**nsertion with **N**eutralized **E**rrors (see Fig. 1). SHINE comprises three innovations: **(i) Manifold-Steered Anchor (MSA) loss**, which leverages pretrained open-domain customization adapters (e.g., IP-Adapter (Ye et al., 2023)) to steer noisy latents toward faithfully representing the reference subject while preserving the structural integrity of the background. **(ii) Degradation-Suppression Guidance (DSG)** that steers sampling away from low-quality distributions. **(iii) Adaptive Background Blending (ABB)** that eliminates visible seams along mask boundaries.

Existing benchmarks primarily comprise background images with a fixed resolution of 512×512 pixels. To evaluate performance across diverse, high-resolution, and demanding scenarios, we introduce *ComplexCompo*, a benchmark that includes varied resolutions, both landscape and portrait orientations, and complex conditions such as low lighting, intense illumination, intricate shadows, and water reflections. Extensive experiments on ComplexCompo and DreamEditBench (Li et al., 2023b) demonstrate that SHINE achieves state-of-the-art (SOTA) performance, surpassing baselines on standard metrics (e.g., DINOv2 (Oquab et al., 2024)) and human-aligned metrics (e.g., DreamSim (Fu et al., 2023), ImageReward (Xu et al., 2023), VisionReward (Xu et al., 2024)).

2 RELATED WORK

This section reviews prior work on image composition. A more comprehensive discussion, covering image composition, general image editing, and subject-driven generation, is offered in Appendix A. Classical image composition splits into sub-tasks (Niu et al., 2021) such as object placement (Azadi et al., 2020; Zhang et al., 2020a), blending (Wu et al., 2019; Zhang et al., 2020b), harmonization (Cao

Figure 2: Image composition from advanced multimodal models under three challenging conditions: backlighting, shadows, and water surfaces. Refer to Appendix H for prompt details.

et al., 2023; Lu et al., 2023b), and shadow generation (Hong et al., 2022; Sheng et al., 2021), typically handled by separate models. Diffusion models have shifted the field toward unified frameworks, either training-based or training-free. Training-based approaches fine-tune diffusion models with curated datasets, adding grounding layers, controllability signals, or identity-preserving supervision from image or video sets (Wang et al., 2025a; Chen et al., 2024c; Yang et al., 2023; Song et al., 2023; Lu et al., 2023c). However, they often bias model priors and struggle with complex lighting due to the lack of large-scale real-world triplets. Training-free approaches avoid retraining by manipulating inversion and attention during inference, enabling flexible test-time adaptation (Yan et al., 2025; Li et al., 2024b; 2023b; Lu et al., 2023d; Pham et al., 2024). Yet these methods remain fragile: strong injections preserve identity but fix unnatural poses, while weaker ones improve realism at the cost of fidelity, reflecting a core trade-off between identity preservation and natural composition.

3 METHOD

Image composition seeks to integrate a subject into a designated area of a background image while preserving the integrity of the surrounding scene. This process typically requires three inputs: (1) one or more reference images of the subject $\{\boldsymbol{x}_1^{\text{subj}}, \boldsymbol{x}_2^{\text{subj}}, \ldots, \boldsymbol{x}_n^{\text{subj}}\}$, (2) a background image $\boldsymbol{x}^{\text{bg}}$, and (3) a user-provided mask $\boldsymbol{M}^{\text{user}}$ specifying the insertion region within the background.

Our framework is built on three core components: Manifold-Steered Anchor (MSA) loss, Degradation-Suppression Guidance (DSG), and Adaptive Background Blending (ABB). Importantly, the design is model-agnostic and requires only standard features of modern generative models: MSA loss assumes that the base model supports either personalization finetuning or provides access to a pretrained personalization adapter, DSG uses self-attention maps, and ABB relies on text-image cross-attention. These mild assumptions enable seamless integration into existing pipelines without architectural changes. We present main results with FLUX, while additional experiments on SDXL (Podell et al., 2024), SD3.5 (Esser et al., 2024), and PixArt (Chen et al.) are provided in Appendix E. The complete algorithm is shown in Algorithm 1.

3.1 NON-INVERSION LATENT PREPARATION

In training-free diffusion-based image composition (Lu et al., 2023d; Pham et al., 2024; Yan et al., 2025; Li et al., 2024b), it is common to start from a noisy latent. Existing training-free frameworks typically rely on image inversion, where the initial noisy latent is constructed by copying the inverted latent of the subject image into a designated region of the background image's inverted latent.

However, this copy-paste strategy constrains the inserted object to the exact pose of its reference image, often leading to contextually inappropriate orientations in the composed result. Moreover, inversion is suboptimal for CFG-distilled models (e.g., FLUX), as it introduces higher inversion errors that compromise subject identity preservation.

To address these limitations, we abandon inversion and instead perform a one-step forward diffusion to obtain the noisy latent. As illustrated in Fig. 3(a), we use a vision-language model (VLM) (Xue et al., 2024; Chen et al., 2024d; Liu et al., 2024) to caption the subject image and leverage this caption, along with an image inpainting model (Li et al., 2024c; Ju et al., 2024; Zhuang et al., 2024; Black Forest Labs, 2024b), to generate the image to which the subject is attached, denoted as $\boldsymbol{x}^{\text{init}}$.

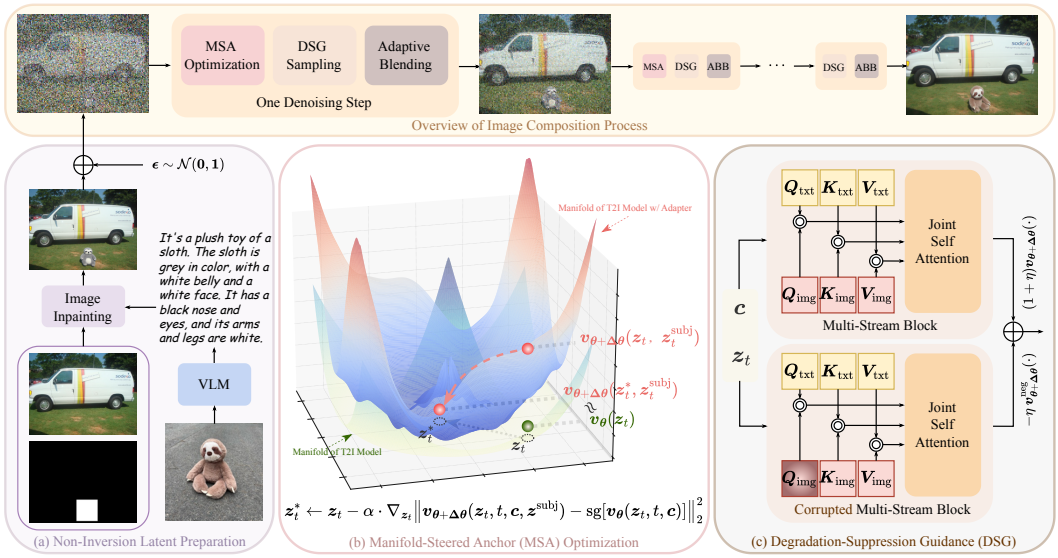

Figure 3: **Overview of the proposed framework. (a)** The noisy latent is created by inpainting the background with a VLM-derived object description, then adding Gaussian noise. **(b)** Manifold-Steered Anchor (MSA) loss guides noisy latents toward faithfully capturing the reference subject (red arrow), while preserving the structural integrity of the background. Concretely, it enforces that the prediction of the optimized latent $\boldsymbol{z}_t^*$ on the adapter-augmented model's manifold remains close to the prediction of the original latent $\boldsymbol{z}_t$ on the base model's manifold. **(c)** Degradation-Suppression Guidance (DSG) constructs a negative velocity pointing toward low-quality regions by blurring $\boldsymbol{Q}_{\text{img}}$ and, in a CFG-like manner, steers the trajectory away from this low-quality distribution.

The noisy latent is encoded in the VAE space as $\boldsymbol{z}^{\text{init}}$ and perturbed to timestep $t \leq T$ via one-step forward diffusion, following the flow matching formulation: $\boldsymbol{z}_t = (1 - \sigma_t)\boldsymbol{z}^{\text{init}} + \sigma_t \boldsymbol{\epsilon}$, where $\boldsymbol{\epsilon} \sim \mathcal{N}(\mathbf{0}, \mathbf{1})$.

3.2 Manifold-Steered Anchor Loss

The Manifold-Steered Anchor (MSA) loss is designed to optimize the noisy latent $\boldsymbol{z}_t$ (from Sec. 3.1) during the denoising process, steering it toward a reference subject while preserving the structural integrity of the original image. The key intuition is to leverage the prior knowledge embedded in pretrained open-domain customization adapters (or alternatively, personalized LoRAs) such as IP-Adapter (Ye et al., 2023), PuLID (Guo et al., 2024), and InstantCharacter (Tao et al., 2025), to intervene directly in the diffusion trajectory. Specifically, the MSA loss is defined as:

$$\min_{\boldsymbol{z}_t} \mathcal{L}_{\text{MSA}}(\boldsymbol{z}_t) = \left\| \boldsymbol{v}_{\boldsymbol{\theta}+\boldsymbol{\Delta\theta}}(\boldsymbol{z}_t, t, \boldsymbol{c}, \boldsymbol{z}^{\text{subj}}) - \text{sg}[\tilde{\boldsymbol{v}}_t] \right\|_2^2, \tag{1}$$

where $\tilde{\boldsymbol{v}}_t \triangleq \boldsymbol{v}_{\boldsymbol{\theta}}(\tilde{\boldsymbol{z}}_t, t, \boldsymbol{c})$ serves as a fixed anchor, preserving the structure of the background image at a given noise level t, with $\tilde{\boldsymbol{z}}_t$ held constant as the original noisy latent. $\boldsymbol{v}_{\boldsymbol{\theta}}(\cdot)$ denotes the velocity predicted by the frozen T2I model $\boldsymbol{\theta}$, while $\boldsymbol{v}_{\boldsymbol{\theta}+\boldsymbol{\Delta\theta}}(\cdot)$ represents the velocity predicted by the a T2I model augmented with an adapter $\Delta\boldsymbol{\theta}$. $\boldsymbol{z}^{\text{subj}}$ is the latent of the subject image. The text prompt $\boldsymbol{c}$ is from the VLM's description of $\boldsymbol{x}^{\text{init}}$, and $\text{sg}[\cdot]$ indicates the stop-gradient operation.

The MSA loss is motivated by the observation that optimizing a latent representation against a frozen generative model implicitly projects the latent onto the model's learned data manifold (Meng et al., 2021; Kim et al., 2022; Graikos et al., 2022; Feng et al., 2023). The generator serves as an implicit prior, guiding gradient descent toward the manifold's basin of attraction.

For instance, when a generative model $\boldsymbol{G}(\boldsymbol{w})$ is trained solely on cat images, its outputs are confined to the cat-image manifold. Thus, approximating a dog image $\boldsymbol{x}_{\text{dog}}$ by solving $\min_{\boldsymbol{w}} \|\boldsymbol{G}(\boldsymbol{w}) - \boldsymbol{x}_{\text{dog}}\|_2^2$ yields $\boldsymbol{G}(\boldsymbol{w}^*)$ that remains a cat image, but with structural features (e.g., pose or outline) aligned to $\boldsymbol{x}_{\text{dog}}$. The result is the projection of the dog image onto the cat manifold, not a genuine dog image.

Analogously, MSA loss is designed to achieve two goals simultaneously. (1) It seeks an optimized noisy latent $\boldsymbol{z}_t^*$ that remains within the manifold of the adapter-augmented model when conditioned on the subject $\boldsymbol{z}^{\text{subj}}$. (2) It encourages the adapter's prediction on this latent $\boldsymbol{z}_t^*$ to align with the base model's prediction on the original latent $\boldsymbol{z}_t$, i.e., $\boldsymbol{v}_{\boldsymbol{\theta}+\boldsymbol{\Delta\theta}}(\boldsymbol{z}_t^*, t, \boldsymbol{c}, \boldsymbol{z}^{\text{subj}}) \approx \boldsymbol{v}_{\boldsymbol{\theta}}(\boldsymbol{z}_t, t, \boldsymbol{c})$ (see Fig. 3(b)).

Figure 4: *Left:* Robustness of FLUX. *Right:* Impacts of blurring different features in FLUX.

Since the velocity prediction of a T2I model on a noisy latent $\boldsymbol{z}_t$ can also be interpreted as a coarse estimate of the clean image that encodes essential structural information (Zheng et al., 2023), this alignment preserves the spatial layout and background details inherited from the original image.

The gradient of $\mathcal{L}_{\text{MSA}}$ with respect to $\boldsymbol{z}_t$ is:

$$\nabla_{\boldsymbol{z}_t}\mathcal{L}_{\text{MSA}}(\boldsymbol{z}_t) = 2\Big(\boldsymbol{v}_{\boldsymbol{\theta}+\boldsymbol{\Delta\theta}}(\boldsymbol{z}_t, t, \boldsymbol{c}, \boldsymbol{z}^{\text{subj}}) - \text{sg}[\tilde{\boldsymbol{v}}_t]\Big)\frac{\partial \boldsymbol{v}_{\boldsymbol{\theta}+\boldsymbol{\Delta\theta}}(\boldsymbol{z}_t, t, \boldsymbol{c})}{\partial \boldsymbol{z}_t}. \tag{2}$$

The Jacobian term necessitates backpropagation through the MMDiT, which is computationally expensive. However, this scenario is analogous to Score Distillation Sampling (SDS) (Poole et al.), where research shows that omitting the Jacobian term yields an effective gradient for optimization with diffusion models. Thus, we adopt the same strategy for optimization.

3.3 Degradation-Suppression Guidance

MSA loss effectively facilitates the insertion of reference objects. However, due to the inherent stochasticity of the denoising and optimization process, the results sometimes suffer from degraded visual quality, manifesting as oversaturated colors and reduced identity consistency (see Fig. 5). To address this, we introduce Degradation-Suppression Guidance (DSG), inspired by negative prompting (Schramowski et al., 2023), defined as:

$$\boldsymbol{v}_t^{\text{dsg}} = \boldsymbol{v}_{\boldsymbol{\theta}+\boldsymbol{\Delta\theta}}(\boldsymbol{z}_t, t, \boldsymbol{c}, \boldsymbol{z}^{\text{subj}}) + \eta\big(\boldsymbol{v}_{\boldsymbol{\theta}+\boldsymbol{\Delta\theta}}(\boldsymbol{z}_t, t, \boldsymbol{c}, \boldsymbol{z}^{\text{subj}}) - \boldsymbol{v}^{\text{neg}}_{\boldsymbol{\theta}+\boldsymbol{\Delta\theta}}(\boldsymbol{z}_t, t, \boldsymbol{c}, \boldsymbol{z}^{\text{subj}})\big), \tag{3}$$

where $\boldsymbol{v}^{\text{neg}}_{\boldsymbol{\theta}+\boldsymbol{\Delta\theta}}$ denotes a negative velocity prediction that guides the generation toward low-quality regions. A key challenge is the design of a meaningful negative velocity prediction $\boldsymbol{v}^{\text{neg}}_{\boldsymbol{\theta}+\boldsymbol{\Delta\theta}}$ within MMDiT-based architectures. In our experiments with FLUX, we observed that using nonsensical text prompts or explicit negative prompts fails to introduce degradation. The generated images remain high-fidelity (Fig. 4(a)), suggesting that text-based negative prompting is ineffective for FLUX.

In our setting, the ideal negative velocity $\boldsymbol{v}^{\text{neg}}_{\boldsymbol{\theta}+\boldsymbol{\Delta\theta}}$ should target directions that preserve the semantic content and spatial layout while lowering perceptual quality. To achieve this, we investigate whether we can manipulate FLUX's internal representations to construct such a targeted degradation signal.

In FLUX, both multi-stream and single-stream blocks compute joint self-attention over concatenated text and image tokens as follows:

$$\boldsymbol{h} = \text{softmax}\Big([\boldsymbol{Q}_{\text{txt}}, \boldsymbol{Q}_{\text{img}}][\boldsymbol{K}_{\text{txt}}, \boldsymbol{K}_{\text{img}}]^{\mathsf{T}}/\sqrt{d_k}\Big)\cdot[\boldsymbol{V}_{\text{txt}}, \boldsymbol{V}_{\text{img}}], \tag{4}$$

where $[\boldsymbol{Q}_{\text{txt}}, \boldsymbol{Q}_{\text{img}}]$ represents the concatenation of text and image queries, and similarly for keys and values. To identify an effective manipulation strategy, we systematically perturb different components in the attention mechanism (i.e., $\boldsymbol{Q}_{\text{txt}}$, $\boldsymbol{K}_{\text{txt}}$, $\boldsymbol{V}_{\text{txt}}$, $\boldsymbol{Q}_{\text{img}}$, $\boldsymbol{K}_{\text{img}}$ and $\boldsymbol{V}_{\text{img}}$) and observe their impact on generation quality.

As shown in Fig. 4(b), our findings are as follows:

1. Blurring $\boldsymbol{Q}_{\text{txt}}$, $\boldsymbol{K}_{\text{txt}}$, or $\boldsymbol{V}_{\text{txt}}$ has negligible impact on semantic fidelity and visual quality.
2. Blurring $\boldsymbol{V}_{\text{img}}$ severely disrupts the output distribution, leading to unintelligible images.
3. Blurring $\boldsymbol{K}_{\text{img}}$ moderately impacts quality, while the image remains visually acceptable.
4. Blurring $\boldsymbol{Q}_{\text{img}}$ yields pronounced degradations while preserving structural integrity, making it the most effective lever for constructing a negative velocity.

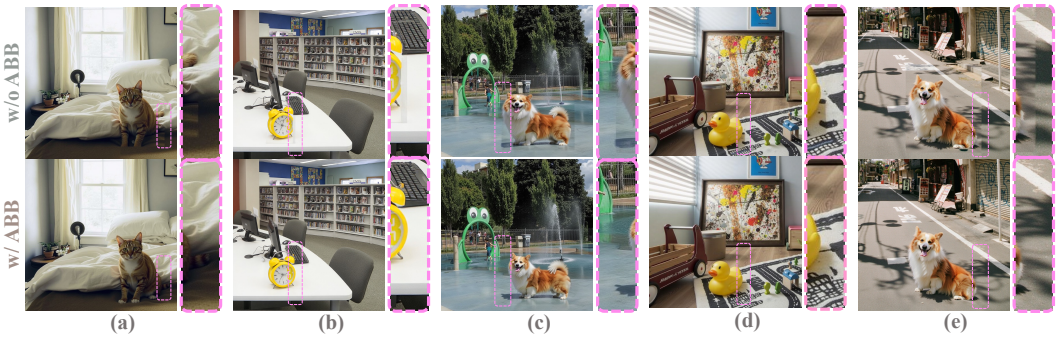

Figure 5: Comparison of rectangular-mask blending and Adaptive Background Blending (ABB). Boundary regions (pink dashed boxes) are enlarged for clarity. Zoom in for details.

Algorithm 1 The Image Composition Process of SHINE.

Input: A background latent $\boldsymbol{z}^{\text{bg}} = \text{VAE}(\boldsymbol{x}^{\text{bg}})$, a subject latent $\boldsymbol{z}^{\text{subj}} = \text{VAE}(\boldsymbol{x}^{\text{subj}})$, a inpainted latent $\boldsymbol{z}^{\text{init}} = \text{VAE}\left(\text{Inpainting}\left[\boldsymbol{x}^{\text{bg}}, \boldsymbol{M}^{\text{user}}, \text{VLM}(\boldsymbol{x}^{\text{subj}})\right]\right)$, a user mask $\boldsymbol{M}^{\text{user}}$.
Output: The composition latent $\boldsymbol{z}_0$.

$\boldsymbol{z}_{t_1} \leftarrow (1-\sigma_{t_1})\boldsymbol{z}^{\text{init}} + \sigma_{t_1}\boldsymbol{\epsilon}$, where $\boldsymbol{\epsilon} \sim \mathcal{N}(\mathbf{0}, \mathbf{1})$
for $t = t_1, \ldots, 0$ **do**
  // Manifold-Steered Anchor (MSA) Optimization
  if $t > \tau$ **then**
    $\tilde{\boldsymbol{v}}_t \leftarrow \boldsymbol{v}_{\boldsymbol{\theta}}(\boldsymbol{z}_t, t, \boldsymbol{c})$
    for $j = 1, \ldots, k$ **do**
      $\boldsymbol{z}_t \leftarrow \boldsymbol{z}_t - \alpha \cdot \boldsymbol{M}^{\text{user}} \odot \nabla_{\boldsymbol{z}_t} \left\| \boldsymbol{v}_{\boldsymbol{\theta}+\boldsymbol{\Delta\theta}}(\boldsymbol{z}_t, t, \boldsymbol{c}, \boldsymbol{z}^{\text{subj}}) - \text{sg}[\tilde{\boldsymbol{v}}_t] \right\|_2^2$
    end for
  end if
  // Degradation-Suppression Guidance (DSG)
  $\boldsymbol{v}_t, \boldsymbol{A}_t \leftarrow \boldsymbol{v}_{\boldsymbol{\theta}+\boldsymbol{\Delta\theta}}(\boldsymbol{z}_t, t, \boldsymbol{c}, \boldsymbol{z}^{\text{subj}})$
  $\boldsymbol{v}_t^{\text{dsg}} \leftarrow \boldsymbol{v}_t + \eta\left(\boldsymbol{v}_t - \boldsymbol{v}^{\text{neg}}_{\boldsymbol{\theta}+\boldsymbol{\Delta\theta}}(\boldsymbol{z}_t, t, \boldsymbol{c}, \boldsymbol{z}^{\text{subj}})\right)$
  $\boldsymbol{z}_{t-1} \leftarrow \boldsymbol{z}_t + (\sigma_{t-1} - \sigma_t)\boldsymbol{v}_t^{\text{dsg}}$
  $\boldsymbol{z}^{\text{bg}}_{t-1} \leftarrow (1-\sigma_{t-1})\boldsymbol{z}^{\text{bg}} + \sigma_{t-1}\boldsymbol{\epsilon}$, where $\boldsymbol{\epsilon} \sim \mathcal{N}(\mathbf{0}, \mathbf{1})$
  // Adaptive Background Blending (ABB)
  $\boldsymbol{M}^{\text{attn}} \leftarrow \text{MaxConnectedComponent}\big(\text{Dilate}(\mathbb{1}(\boldsymbol{A}_t \geq \gamma))\big)$
  $\hat{\boldsymbol{M}} \leftarrow \mathbb{1}\{t > \tau\}\, \boldsymbol{M}^{\text{attn}} + \mathbb{1}\{t \leq \tau\}\, \boldsymbol{M}^{\text{user}}$
  $\boldsymbol{z}_{t-1} \leftarrow \hat{\boldsymbol{M}} \odot \boldsymbol{z}_{t-1} + \left(1 - \hat{\boldsymbol{M}}\right) \odot \boldsymbol{z}^{\text{bg}}_{t-1}$
end for
return $\boldsymbol{z}_0$

Based on these insights, we construct the negative velocity prediction $\boldsymbol{v}^{\text{neg}}_{\boldsymbol{\theta}+\Delta\boldsymbol{\theta}}$ in Eqn. 3 by blurring $\boldsymbol{Q}_{\text{img}}$ within FLUX (see Fig. 3(c)). Moreover, we show that blurring $\boldsymbol{Q}_{\text{img}}$ is mathematically equivalent to blurring the self-attention weights, whereas blurring $\boldsymbol{K}_{\text{img}}$ or $\boldsymbol{V}_{\text{img}}$ is not (see Appendix C for the proof). This equivalence is consistent with the fact that attenuating self-attention activations suppresses informative interactions and thus degrades image quality (Lu et al., 2024).

3.4 Adaptive Background Blending

Previous methods typically rely on the user-provided mask $\boldsymbol{M}^{\text{user}}$ to preserve the background during each denoising step, blending as $\boldsymbol{z}'_t = \boldsymbol{M}^{\text{user}} \odot \boldsymbol{z}_t + (1 - \boldsymbol{M}^{\text{user}}) \odot \boldsymbol{z}^{\text{bg}}_t$, but this often introduces visible seams along mask boundaries (see the first row of Fig. 5).

To address this limitation, we propose Adaptive Background Blending (ABB), defined as

$$\boldsymbol{z}'_t = \hat{\boldsymbol{M}} \odot \boldsymbol{z}_t + \left(1 - \hat{\boldsymbol{M}}\right) \odot \boldsymbol{z}^{\text{bg}}_t, \qquad \hat{\boldsymbol{M}} = \mathbb{1}\{t > \tau\}\, \mathcal{D}(\boldsymbol{M}^{\text{attn}}) + \mathbb{1}\{t \leq \tau\}\, \boldsymbol{M}^{\text{user}}, \tag{5}$$

where $\boldsymbol{M}^{\text{user}}$ is the user mask, while $\boldsymbol{M}^{\text{attn}}$ is derived by binarizing the cross-attention maps corresponding to subject tokens. These maps can be obtained by either averaging across layers or select-

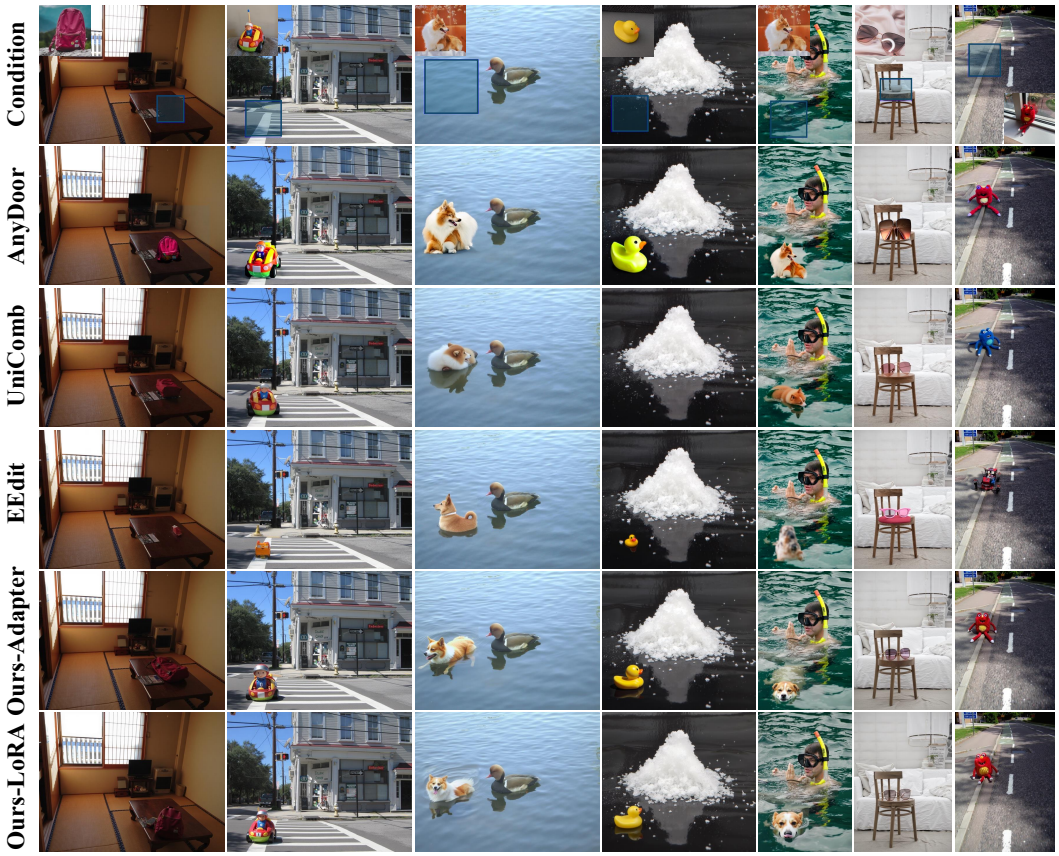

Figure 6: Qualitative comparison of our method with multiple baselines in challenging scenarios, **drawn from our benchmark dataset**. More qualitative comparisons are available in Appendix O.

ing the most informative layer via a lightweight analysis (details in Appendix D). The operator $\mathcal{D}(\cdot)$ performs dilation and extracts the largest connected component, ensuring robustness to noise.

Compared to $\boldsymbol{M}^{\text{user}}$, $\boldsymbol{M}^{\text{attn}}$ is more spatially precise, particularly for elongated or irregularly shaped objects that do not fully occupy a rectangular region. As illustrated in the second row of Fig. 5, our method produces smoother transitions by replacing the rigid user mask with the semantically guided mask. This refinement better preserves the surrounding scene, enabling seamless integration between generated content and the original background. However, applying this method throughout the denoising process may truncate object shadows or reflections. Through empirical evaluation, we find that leveraging $\boldsymbol{M}^{\text{attn}}$ during the initial denoising steps $(t > \tau)$ sufficiently mitigates visible seams along mask boundaries, ensuring high-fidelity scene coherence.

4 Experiments

4.1 Experimental Setup

Benchmark. Current benchmarks primarily consist of background images with a fixed resolution of 512×512 pixels. To assess performance across diverse, high-resolution, and complex scenarios, we introduce *ComplexCompo*, a benchmark built upon DreamEditBench (Li et al., 2023b). DreamEditBench includes 220 (subject, background, bounding box) pairs designed for 512×512 resolution. In contrast, ComplexCompo features 300 composition pairs with varying resolutions, encompassing both landscape and portrait orientations, and incorporates challenging conditions such as low lighting, intense illumination, intricate shadows, and water reflections. The background images are sourced from OpenImage (Kuznetsova et al., 2020). Further details are provided in Appendix G.

Metrics. Previous methods primarily adapt CLIP-I (Radford et al., 2021) and DINOv2 (Oquab et al., 2024) to assess subject identity consistency. However, these features capture high-level semantic information that may not fully align with human perception of finer-grained attributes. Thus, we further incorporate instance retrieval features (IRF) from (Shao & Cui, 2022) and DreamSim (Fu et al., 2023), which better align with human judgments. An analysis of identity consistency metrics is provided in Appendix I. For overall image quality, we use ImageReward (IR) (Xu et al., 2023)

Table 1: Comparison of composition performance across two benchmarks. The best result in each column is highlighted in **bold**, while the second-best is underlined. Metrics shown in pink are those specifically trained to better align with human preferences. Abbreviations: IRF= Instance Retrieval Features; IR = ImageReward; VR = VisionReward; URE = UnifiedReward-Edit-qwen3vl-8b.

Bench	Method	Training -Free	Base Model	External Model	Subject Identity Consistency				Background		Image Quality			
					CLIP-I ↑	DINOv2 ↑	IRF ↑	DreamSim ↓	LPIPS ↓	SSIM ↑	IR ↑	VR ↑	HPS ↑	URE ↑
Dream-Edit-Bench (220)	Flux.1 Fill (Black Forest Labs, 2024b)	✘	FLUX	-	0.7328	0.6745	0.5754	0.5233	0.0166	0.9076	0.5577	3.5997	8.6432	21.5812
	MADD (He et al., 2024)	✘	SD	DINO	0.7118	0.6279	0.4333	0.5810	0.0604	0.8182	-0.2545	2.7011	1.2443	13.8148
	ObjectStitch (Song et al., 2023)	✘	SD	VIT	0.7567	0.6930	0.5525	0.5093	0.0190	0.8316	0.0791	3.2416	7.4529	19.1886
	DreamCom (Lu et al., 2023c)	✘	SD	LoRA	0.7414	0.6749	0.5597	0.5626	0.0200	0.8283	0.1873	3.5053	5.9324	19.9296
	AnyDoor (Chen et al., 2024c)	✘	SD	DINO	**0.8183**	0.7283	0.7714	0.3764	0.0251	0.8894	0.4511	3.3946	8.4867	19.0989
	UniCombine (Wang et al., 2025a)	✘	FLUX	LoRA	0.8058	0.7332	0.7579	0.3984	0.0050	0.9397	0.4565	3.6108	8.8415	21.7080
	PBE (Yang et al., 2023)	✘	SD	-	0.7742	0.7040	0.5845	0.4985	0.0197	0.8287	0.2083	3.3482	8.3789	20.2137
	TIGIC (Li et al., 2024b)	✔	SD	-	0.7226	0.6718	0.4711	0.6108	0.0584	0.8153	-0.1332	2.9873	5.2676	17.1000
	TALE (Pham et al., 2024)	✔	SD	-	0.7329	0.6604	0.5007	0.6176	0.0392	0.8251	-0.1502	3.1349	6.3773	18.0784
	TF-ICON (Lu et al., 2023d)	✔	SD	-	0.7479	0.6865	0.5179	0.5441	0.0582	0.8111	0.0816	3.2823	7.2643	18.2716
	DreamEdit (Li et al., 2023b)	✔	SD	LoRA, VIT	0.7703	0.7151	0.6147	0.5047	0.0140	**0.9775**	0.1744	3.1775	6.0250	15.7636
	EEdit (Yan et al., 2025)	✔	FLUX	-	0.6998	0.6590	0.4438	0.6160	**0.0039**	0.9475	0.0216	3.3606	6.6689	19.5603
	Ours-Adapter	✔	FLUX	Adapter	0.8086	0.7415	0.7702	0.3730	0.0236	0.8959	0.5709	**3.6234**	**8.8861**	**22.0182**
	Ours-LoRA	✔	FLUX	LoRA	0.8125	**0.7452**	**0.7900**	**0.3577**	0.0271	0.8847	**0.5906**	3.6161	8.8688	21.9421
Complex-Compo (300)	Flux.1 Fill (Black Forest Labs, 2024b)	✘	FLUX	-	0.7108	0.6475	0.5466	0.6018	0.0232	0.7442	0.4088	3.5737	8.7376	19.7712
	MADD (He et al., 2024)	✘	SD	DINO	0.6780	0.5993	0.3638	0.5979	0.0781	0.5658	-0.0088	2.6582	5.9673	13.0567
	ObjectStitch (Song et al., 2023)	✘	SD	VIT	0.7608	0.7077	0.5513	0.4717	0.0388	0.6357	0.2482	3.4411	8.8389	18.8283
	DreamCom (Lu et al., 2023c)	✘	SD	LoRA	0.648	0.5692	0.2788	0.8192	0.0389	0.6342	-0.0778	3.4409	7.9884	18.6143
	AnyDoor (Chen et al., 2024c)	✘	SD	DINO	0.7982	0.7052	0.7319	0.4493	0.0299	0.7262	0.3804	3.3787	8.9760	18.3550
	UniCombine (Wang et al., 2025a)	✘	FLUX	LoRA	0.7361	0.6552	0.5380	0.5682	0.0237	0.7077	0.2470	3.5454	8.8999	19.8529
	PBE (Yang et al., 2023)	✘	SD	-	0.7537	0.6802	0.5189	0.5187	0.0397	0.6321	0.2139	3.4310	8.5923	18.9507
	TIGIC (Li et al., 2024b)	✔	SD	-	0.6913	0.6329	0.3848	0.6549	0.0929	0.6228	-0.131	2.8898	7.6630	16.4301
	TALE (Pham et al., 2024)	✔	SD	-	0.6816	0.6151	0.3799	0.6773	0.059	0.6334	0.0783	3.4498	8.7351	18.7567
	TF-ICON (Lu et al., 2023d)	✔	SD	-	0.6987	0.6435	0.4167	0.6030	0.0815	0.6216	0.1798	3.4323	9.3258	18.2366
	DreamEdit (Li et al., 2023b)	✔	SD	LoRA, VIT	0.7314	0.6722	0.5069	0.5670	0.0468	0.7201	0.1212	3.2531	8.0434	15.8934
	EEdit (Yan et al., 2025)	✔	FLUX	-	0.6713	0.6153	0.3797	0.6821	**0.0226**	0.7107	0.1433	3.5009	8.7835	19.7348
	Ours-Adapter	✔	FLUX	Adapter	0.7721	0.7107	0.6764	0.4294	0.0404	**0.7789**	0.4090	**3.6020**	9.6485	20.7349
	Ours-LoRA	✔	FLUX	LoRA	**0.7999**	**0.7384**	**0.7659**	**0.3542**	0.0430	0.7634	**0.4246**	3.5951	**9.8418**	**21.0326**

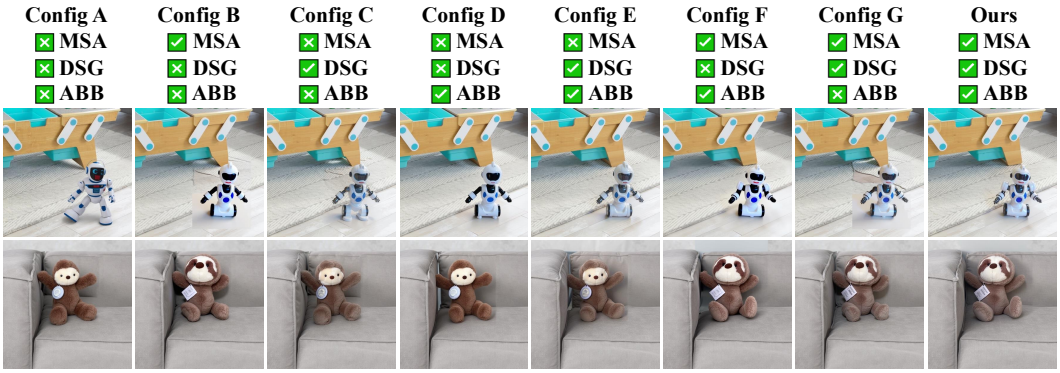

Figure 7: Qualitative ablation study comparing different variants of our framework.

and VisionReward (VR) (Xu et al., 2024), fine-grained reward models that more accurately reflect human preferences. To more comprehensively evaluate composition quality, we further include three UnifiedReward variants (Wang et al., 2025b;c) and HPSv3 (Ma et al., 2025b) in Appendix L. Background consistency is measured using LPIPS (Zhang et al., 2018) and SSIM (Wang et al., 2004).

Implementation Details. In our experiment, we used FLUX.1-dev, a 12B-parameter flow matching model, as the base model, combined with InstantCharacter (Tao et al., 2025) as the adapter (Additional results on SDXL, SD3.5, and PixArt are presented in Appendix E). Our approach also supports per-concept LoRA (Hu et al.), which requires test-time tuning (Ruiz et al., 2023) but delivers superior identity consistency compared to an open-domain adapter, making it ideal for scenarios demanding precise identity preservation. The denoising schedule consists of 20 steps, with the inpainted image perturbed to timestep 15 and denoising initiated from that point. We use Flux.1 Fill (Black Forest Labs, 2024b) as the inpainting model and BLIP-3 (Xue et al., 2024) as the VLM. Additional details and hyperparameters are provided in Appendix J.

4.2 Experimental Results

We compare our method with two categories of baselines: **(1) Training-based methods (6 in total)**: UniCombine (Wang et al., 2025a), AnyDoor (Chen et al., 2024c), Paint by Example (PBE) (Yang et al., 2023), ObjectStitch (Song et al., 2023), MADD (He et al., 2024), and DreamCom (Lu et al., 2023c); **(2) Training-free methods (5 in total)**: EEdit (Yan et al., 2025), TIGIC (Li et al., 2024b), DreamEdit (Li et al., 2023b), TF-ICON (Lu et al., 2023d), and TALE (Pham et al., 2024).

As shown in Tab. 1, both variants of our method surpass all baselines on DreamEditBench across human preference aligned metrics (i.e., DreamSim, IR, VR), which are the most critical indicators of quality. For background-related metrics, all methods achieve comparable results, with differences so small they are imperceptible to the human eye. On the more challenging ComplexCompo dataset, which includes non-square resolutions and intricate scenes, most methods experience a notable per-

Figure 8: Composition inherit erroneous colors if the inpainting prompt specifies an incorrect color.

Table 2: Ablation study examining the impact of key components on DreamEditBench.

Method	MSA	DSG	ABB	Subject Identity Consistency				Background		Image Quality	
				CLIP-I	DINOv2	IRF	DreamSim	LPIPS	SSIM	IR	VR
Config A	✘	✘	✘	0.7328	0.6745	0.5754	0.5233	**0.0166**	**0.9076**	0.5577	3.5997
Config B	✔	✘	✘	0.7814	0.7204	0.7414	0.3951	0.0172	0.9075	0.5455	3.5952
Config C	✘	✔	✘	0.7528	0.6941	0.6533	0.4436	0.0178	0.9038	0.5633	3.6130
Config D	✘	✘	✔	0.7421	0.6814	0.6158	0.5127	0.0210	0.9010	0.5595	3.6109
Config E	✘	✔	✔	0.7481	0.6987	0.6647	0.4317	0.0218	0.8971	**0.5850**	**3.6277**
Config F	✔	✘	✔	0.8084	**0.7429**	0.7609	0.3756	0.0231	0.8991	0.5459	3.6023
Config G	✔	✔	✘	0.8077	0.7375	0.7589	0.3762	0.0182	0.9037	0.5745	3.6191
Ours-Adapter	✔	✔	✔	**0.8086**	0.7415	**0.7702**	**0.3730**	0.0236	0.8959	0.5709	3.6232

formance drop, yet our approach consistently remains the top performer. From Fig. 6, it is evident that while AnyDoor achieves high scores on many identity metrics, the model tends to copy and paste the subject into the scene, resulting in unnatural compositions and lower image quality scores. In contrast, our method excels at naturally composing objects in challenging conditions (e.g., low-light settings, water surfaces, and scenes with complex shadows). Appendix F provides user study.

4.3 Ablation Study

We validate our design choices through ablation (see Tab. 2 and Fig. 7). The results highlight three key insights. First, MSA loss notably improves subject identity consistency. Second, DSG boosts IR and VR scores by steering denoising away from low-quality regions. Finally, ABB effectively suppresses visible seams along mask boundaries. While this improvement is readily apparent in visual comparisons (Figs. 5, 7), it is less well captured by quantitative metrics, since LPIPS and SSIM primarily assess structural similarity rather than perceptual smoothness.

5 Conclusion

We introduced SHINE, a training-free framework for seamless and high-fidelity image composition with pretrained T2I models. SHINE integrates Manifold-Steered Anchor Loss, Degradation-Suppression Guidance, and Adaptive Background Blending to ensure precise subject placement and artifact-free synthesis across diverse resolutions and lighting conditions. To enable rigorous evaluation, we proposed ComplexCompo, a benchmark for challenging composition scenarios. SHINE achieves state-of-the-art results on both ComplexCompo and DreamEditBench.

Limitations. Our method reliably converges to the correct subject identity through MSA optimization even when the inpainted subject's appearance deviates substantially from the reference (see Fig. 8(a)). However, when the inpainting prompt specifies an incorrect color, the final inpainted result tends to inherit and preserve this erroneous color (see Fig. 8(b)). On the other hand, the similarity between the inserted object and the user-provided object depends on the quality of the customization adapter used. As shown in Tab. 1, because LoRA performs test-time tuning for individual concepts, it generates subjects that are more similar to the target than those produced by pretrained open-domain customization adapters, resulting in higher subject identity consistency metrics in the composition. While current customization adapters already perform well, the potential of our method will continue to improve as advancements are made in the field of open-domain customization adapters.

Ethics Statement

Our framework provides an accessible way for people without professional artistic skills to create image compositions. While this technology offers significant benefits, it also carries the risk of misuse for malicious purposes, such as harassment or spreading misinformation. Additionally, our framework relies on pretrained large-scale T2I models, which may inadvertently introduce social and cultural biases. Therefore, using these models raises ethical concerns and requires careful consideration. We therefore urge users to exercise caution and use this tool responsibly for appropriate purposes only.

Reproducibility Statement

We have taken several measures to ensure the reproducibility of our results. Algorithm 1 presents the pseudocode of our method. Details of the implementation for the main experiments are provided in Sec. 4.1, while the hyperparameter configurations are listed in Appendix J. The source code and the ComplexCompo dataset will be released publicly. This work adheres to the reproducibility requirements set by ICLR.

References

Grok 4, 2025. URL https://x.ai/news/grok-4.

Samaneh Azadi, Deepak Pathak, Sayna Ebrahimi, and Trevor Darrell. Compositional gan: Learning image-conditional binary composition. *International Journal of Computer Vision*, 128(10):2570–2585, 2020.

Black Forest Labs. Flux.1 [dev]. https://huggingface.co/black-forest-labs/FLUX.1-dev, 2024a.

Black Forest Labs. Flux.1 fill [dev]. https://huggingface.co/black-forest-labs/FLUX.1-Fill-dev, 2024b.

Black Forest Labs. Flux.1 [schnell]. https://huggingface.co/black-forest-labs/FLUX.1-schnell, 2024c.

Tim Brooks, Aleksander Holynski, and Alexei A Efros. Instructpix2pix: Learning to follow image editing instructions. In *Proceedings of the IEEE/CVF conference on computer vision and pattern recognition*, pp. 18392–18402, 2023.

Gemma Canet Tarrés, Zhe Lin, Zhifei Zhang, Jianming Zhang, Yizhi Song, Dan Ruta, Andrew Gilbert, John Collomosse, and Soo Ye Kim. Thinking outside the bbox: Unconstrained generative object compositing. In *European Conference on Computer Vision*, pp. 476–495. Springer, 2024.

Junyan Cao, Yan Hong, and Li Niu. Painterly image harmonization in dual domains. In *Proceedings of the AAAI Conference on Artificial Intelligence*, volume 37, pp. 268–276, 2023.

Bor-Chun Chen and Andrew Kae. Toward realistic image compositing with adversarial learning. In *Proceedings of the IEEE/CVF Conference on Computer Vision and Pattern Recognition*, pp. 8415–8424, 2019.

Jiaxuan Chen, Bo Zhang, Qingdong He, Jinlong Peng, and Li Niu. Mureobjectstitch: Multi-reference image composition. *arXiv preprint arXiv:2411.07462*, 2024a.

Junsong Chen, YU Jincheng, GE Chongjian, Lewei Yao, Enze Xie, Zhongdao Wang, James Kwok, Ping Luo, Huchuan Lu, and Zhenguo Li. Pixart-α: Fast training of diffusion transformer for photorealistic text-to-image synthesis. In *The Twelfth International Conference on Learning Representations*.

Liang Chen, Shuai Bai, Wenhao Chai, Weichu Xie, Haozhe Zhao, Leon Vinci, Junyang Lin, and Baobao Chang. Multimodal representation alignment for image generation: Text-image interleaved control is easier than you think, 2025.

Xi Chen, Yutong Feng, Mengting Chen, Yiyang Wang, Shilong Zhang, Yu Liu, Yujun Shen, and Hengshuang Zhao. Zero-shot image editing with reference imitation. *Advances in Neural Information Processing Systems*, 37:84010–84032, 2024b.

Xi Chen, Lianghua Huang, Yu Liu, Yujun Shen, Deli Zhao, and Hengshuang Zhao. Anydoor: Zero-shot object-level image customization. In *Proceedings of the IEEE/CVF conference on computer vision and pattern recognition*, pp. 6593–6602, 2024c.

Zhe Chen, Jiannan Wu, Wenhai Wang, Weijie Su, Guo Chen, Sen Xing, Muyan Zhong, Qinglong Zhang, Xizhou Zhu, Lewei Lu, et al. Internvl: Scaling up vision foundation models and aligning for generic visual-linguistic tasks. In *Proceedings of the IEEE/CVF conference on computer vision and pattern recognition*, pp. 24185–24198, 2024d.

Zhekai Chen, Wen Wang, Zhen Yang, Zeqing Yuan, Hao Chen, and Chunhua Shen. Freecompose: Generic zero-shot image composition with diffusion prior. In *European Conference on Computer Vision*, pp. 70–87. Springer, 2024e.

Wenyan Cong, Jianfu Zhang, Li Niu, Liu Liu, Zhixin Ling, Weiyuan Li, and Liqing Zhang. Dovenet: Deep image harmonization via domain verification. In *Proceedings of the IEEE/CVF Conference on Computer Vision and Pattern Recognition*, pp. 8394–8403, 2020.

Xiaodong Cun and Chi-Man Pun. Improving the harmony of the composite image by spatial-separated attention module. *IEEE Transactions on Image Processing*, 29:4759–4771, 2020.

Patrick Esser, Sumith Kulal, Andreas Blattmann, Rahim Entezari, Jonas Müller, Harry Saini, Yam Levi, Dominik Lorenz, Axel Sauer, Frederic Boesel, et al. Scaling rectified flow transformers for high-resolution image synthesis. In *Forty-first international conference on machine learning*, 2024.

Berthy T Feng, Jamie Smith, Michael Rubinstein, Huiwen Chang, Katherine L Bouman, and William T Freeman. Score-based diffusion models as principled priors for inverse imaging. In *Proceedings of the IEEE/CVF International Conference on Computer Vision*, pp. 10520–10531, 2023.

Stephanie Fu, Netanel Tamir, Shobhita Sundaram, Lucy Chai, Richard Zhang, Tali Dekel, and Phillip Isola. Dreamsim: Learning new dimensions of human visual similarity using synthetic data. *Advances in Neural Information Processing Systems*, 36:50742–50768, 2023.

Rinon Gal, Yuval Alaluf, Yuval Atzmon, Or Patashnik, Amit Haim Bermano, Gal Chechik, and Daniel Cohen-or. An image is worth one word: Personalizing text-to-image generation using textual inversion. In *The Eleventh International Conference on Learning Representations*, 2022.

Google Gemini2.5. Introducing gemini 2.5 flash image, our state-of-the-art image model, 2025. URL https://developers.googleblog.com/en/introducing-gemini-2-5-flash-image/.

Alexandros Graikos, Nikolay Malkin, Nebojsa Jojic, and Dimitris Samaras. Diffusion models as plug-and-play priors. *Advances in Neural Information Processing Systems*, 35:14715–14728, 2022.

Zinan Guo, Yanze Wu, Chen Zhuowei, Peng Zhang, Qian He, et al. Pulid: Pure and lightning id customization via contrastive alignment. *Advances in neural information processing systems*, 37: 36777–36804, 2024.

Ligong Han, Yinxiao Li, Han Zhang, Peyman Milanfar, Dimitris Metaxas, and Feng Yang. Svdiff: Compact parameter space for diffusion fine-tuning. In *Proceedings of the IEEE/CVF International Conference on Computer Vision*, pp. 7323–7334, 2023.

Zhen Han, Zeyinzi Jiang, Yulin Pan, Jingfeng Zhang, Chaojie Mao, Chen-Wei Xie, Yu Liu, and Jingren Zhou. Ace: All-round creator and editor following instructions via diffusion transformer. In *The Thirteenth International Conference on Learning Representations*.

Jixuan He, Wanhua Li, Ye Liu, Junsik Kim, Donglai Wei, and Hanspeter Pfister. Affordance-aware object insertion via mask-aware dual diffusion. *arXiv preprint arXiv:2412.14462*, 2024.

HiDream-ai. Hidream-e1. https://github.com/HiDream-ai/HiDream-E1, 2025.

Yan Hong, Li Niu, and Jianfu Zhang. Shadow generation for composite image in real-world scenes. In *Proceedings of the AAAI Conference on Artificial Intelligence*, volume 36, pp. 914–922, 2022.

Edward J Hu, Phillip Wallis, Zeyuan Allen-Zhu, Yuanzhi Li, Shean Wang, Lu Wang, Weizhu Chen, et al. Lora: Low-rank adaptation of large language models. In *International Conference on Learning Representations*.

Junjia Huang, Pengxiang Yan, Jiyang Liu, Jie Wu, Zhao Wang, Yitong Wang, Liang Lin, and Guanbin Li. Dreamfuse: Adaptive image fusion with diffusion transformer. *arXiv preprint arXiv:2504.08291*, 2025.

Yuzhou Huang, Liangbin Xie, Xintao Wang, Ziyang Yuan, Xiaodong Cun, Yixiao Ge, Jiantao Zhou, Chao Dong, Rui Huang, Ruimao Zhang, and Ying Shan. Smartedit: Exploring complex instruction-based image editing with multimodal large language models. *2024 IEEE/CVF Conference on Computer Vision and Pattern Recognition (CVPR)*, pp. 8362–8371, 2024.

Junha Hyung, Jaeyo Shin, and Jaegul Choo. Magicapture: High-resolution multi-concept portrait customization. In *Proceedings of the AAAI Conference on Artificial Intelligence*, volume 38, pp. 2445–2453, 2024.

Yifan Jiang, He Zhang, Jianming Zhang, Yilin Wang, Zhe Lin, Kalyan Sunkavalli, Simon Chen, Sohrab Amirghodsi, Sarah Kong, and Zhangyang Wang. Ssh: A self-supervised framework for image harmonization. In *Proceedings of the IEEE/CVF International Conference on Computer Vision*, pp. 4832–4841, 2021.

Jian Jin, Yang Shen, Xinyang Zhao, Zhenyong Fu, and Jian Yang. Unicanvas: Affordance-aware unified real image editing via customized text-to-image generation. *International Journal of Computer Vision*, pp. 1–25, 2025.

Xuan Ju, Xian Liu, Xintao Wang, Yuxuan Bian, Ying Shan, and Qiang Xu. Brushnet: A plug-and-play image inpainting model with decomposed dual-branch diffusion. In *European Conference on Computer Vision*, pp. 150–168. Springer, 2024.

Gwanghyun Kim, Taesung Kwon, and Jong Chul Ye. Diffusionclip: Text-guided diffusion models for robust image manipulation. In *Proceedings of the IEEE/CVF conference on computer vision and pattern recognition*, pp. 2426–2435, 2022.

Nupur Kumari, Bingliang Zhang, Richard Zhang, Eli Shechtman, and Jun-Yan Zhu. Multi-concept customization of text-to-image diffusion. In *Proceedings of the IEEE/CVF Conference on Computer Vision and Pattern Recognition*, pp. 1931–1941, 2023.

Alina Kuznetsova, Hassan Rom, Neil Alldrin, Jasper Uijlings, Ivan Krasin, Jordi Pont-Tuset, Shahab Kamali, Stefan Popov, Matteo Malloci, Alexander Kolesnikov, et al. The open images dataset v4: Unified image classification, object detection, and visual relationship detection at scale. *International journal of computer vision*, 128(7):1956–1981, 2020.

Dongxu Li, Junnan Li, and Steven Hoi. Blip-diffusion: Pre-trained subject representation for controllable text-to-image generation and editing. *Advances in Neural Information Processing Systems*, 36, 2024a.

Junnan Li, Dongxu Li, Silvio Savarese, and Steven Hoi. Blip-2: bootstrapping language-image pre-training with frozen image encoders and large language models. In *Proceedings of the 40th International Conference on Machine Learning*, ICML'23. JMLR.org, 2023a.

Pengzhi Li, Qiang Nie, Ying Chen, Xi Jiang, Kai Wu, Yuhuan Lin, Yong Liu, Jinlong Peng, Chengjie Wang, and Feng Zheng. Tuning-free image customization with image and text guidance. In *European Conference on Computer Vision*, pp. 233–250. Springer, 2024b.

Tianle Li, Max Ku, Cong Wei, and Wenhu Chen. Dreamedit: Subject-driven image editing. *Transactions on Machine Learning Research*, 2023b.

Yaowei Li, Yuxuan Bian, Xuan Ju, Zhaoyang Zhang, Junhao Zhuang, Ying Shan, Yuexian Zou, and Qiang Xu. Brushedit: All-in-one image inpainting and editing. *arXiv preprint arXiv:2412.10316*, 2024c.

Yuheng Li, Haotian Liu, Qingyang Wu, Fangzhou Mu, Jianwei Yang, Jianfeng Gao, Chunyuan Li, and Yong Jae Lee. Gligen: Open-set grounded text-to-image generation. In *Proceedings of the IEEE/CVF conference on computer vision and pattern recognition*, pp. 22511–22521, 2023c.

Chen-Hsuan Lin, Ersin Yumer, Oliver Wang, Eli Shechtman, and Simon Lucey. St-gan: Spatial transformer generative adversarial networks for image compositing. In *Proceedings of the IEEE Conference on Computer Vision and Pattern Recognition*, pp. 9455–9464, 2018.

Daquan Liu, Chengjiang Long, Hongpan Zhang, Hanning Yu, Xinzhi Dong, and Chunxia Xiao. Arshadowgan: Shadow generative adversarial network for augmented reality in single light scenes. In *Proceedings of the IEEE/CVF Conference on Computer Vision and Pattern Recognition*, pp. 8139–8148, 2020.

Haotian Liu, Chunyuan Li, Yuheng Li, and Yong Jae Lee. Improved baselines with visual instruction tuning. In *Proceedings of the IEEE/CVF Conference on Computer Vision and Pattern Recognition*, pp. 26296–26306, 2024.

Cheng Lu, Yuhao Zhou, Fan Bao, Jianfei Chen, Chongxuan Li, and Jun Zhu. Dpm-solver: A fast ode solver for diffusion probabilistic model sampling in around 10 steps. *Advances in Neural Information Processing Systems*, 35:5775–5787, 2022.

Haoming Lu, Hazarapet Tunanyan, Kai Wang, Shant Navasardyan, Zhangyang Wang, and Humphrey Shi. Specialist diffusion: Plug-and-play sample-efficient fine-tuning of text-to-image diffusion models to learn any unseen style. In *Proceedings of the IEEE/CVF Conference on Computer Vision and Pattern Recognition*, pp. 14267–14276, 2023a.

Lingxiao Lu, Jiangtong Li, Junyan Cao, Li Niu, and Liqing Zhang. Painterly image harmonization using diffusion model. In *Proceedings of the 31st ACM International Conference on Multimedia*, pp. 233–241, 2023b.

Lingxiao Lu, Jiangtong Li, Bo Zhang, and Li Niu. Dreamcom: Finetuning text-guided inpainting model for image composition. *arXiv preprint arXiv:2309.15508*, 2023c.

Pengqi Lu. Qwen2vl-flux: Unifying image and text guidance for controllable image generation, 2024. URL https://github.com/erwold/qwen2vl-flux.

Shilin Lu, Yanzhu Liu, and Adams Wai-Kin Kong. Tf-icon: Diffusion-based training-free cross-domain image composition. In *Proceedings of the IEEE/CVF International Conference on Computer Vision*, pp. 2294–2305, 2023d.

Shilin Lu, Zilan Wang, Leyang Li, Yanzhu Liu, and Adams Wai-Kin Kong. Mace: Mass concept erasure in diffusion models. In *Proceedings of the IEEE/CVF Conference on Computer Vision and Pattern Recognition*, pp. 6430–6440, 2024.

Jian Ma, Qirong Peng, Xu Guo, Chen Chen, Haonan Lu, and Zhenyu Yang. X2i: Seamless integration of multimodal understanding into diffusion transformer via attention distillation. In *Proceedings of the IEEE/CVF International Conference on Computer Vision*, pp. 16733–16744, 2025a.

Yuhang Ma, Xiaoshi Wu, Keqiang Sun, and Hongsheng Li. Hpsv3: Towards wide-spectrum human preference score. In *Proceedings of the IEEE/CVF International Conference on Computer Vision*, pp. 15086–15095, 2025b.

Chaojie Mao, Jingfeng Zhang, Yulin Pan, Zeyinzi Jiang, Zhen Han, Yu Liu, and Jingren Zhou. Ace++: Instruction-based image creation and editing via context-aware content filling. *arXiv preprint arXiv:2501.02487*, 2025.

Chenlin Meng, Yutong He, Yang Song, Jiaming Song, Jiajun Wu, Jun-Yan Zhu, and Stefano Ermon. Sdedit: Guided image synthesis and editing with stochastic differential equations. In *International Conference on Learning Representations*, 2021.

Li Ming, Gu Xin, Chen Fan, Xing Xiaoying, Wen Longyin, Chen Chen, and Zhu Sijie. Superedit: Rectifying and facilitating supervision for instruction-based image editing. *arXiv preprint arXiv:2505.02370*, 2025.

Ron Mokady, Amir Hertz, Kfir Aberman, Yael Pritch, and Daniel Cohen-Or. Null-text inversion for editing real images using guided diffusion models. In *Proceedings of the IEEE/CVF conference on computer vision and pattern recognition*, pp. 6038–6047, 2023.

Li Niu, Wenyan Cong, Liu Liu, Yan Hong, Bo Zhang, Jing Liang, and Liqing Zhang. Making images real again: A comprehensive survey on deep image composition. *arXiv preprint arXiv:2106.14490*, 2021.

OpenAI. Introducing gpt-5, 2025. URL https://openai.com/index/introducing-gpt-5/.

Maxime Oquab, Timothée Darcet, Théo Moutakanni, Huy Vo, Marc Szafraniec, Vasil Khalidov, Pierre Fernandez, Daniel Haziza, Francisco Massa, Alaaeldin El-Nouby, et al. Dinov2: Learning robust visual features without supervision. *Transactions on Machine Learning Research Journal*, 2024.

Xichen Pan, Satya Narayan Shukla, Aashu Singh, Zhuokai Zhao, Shlok Kumar Mishra, Jialiang Wang, Zhiyang Xu, Jiuhai Chen, Kunpeng Li, Felix Juefei-Xu, et al. Transfer between modalities with metaqueries. *arXiv preprint arXiv:2504.06256*, 2025.

William Peebles and Saining Xie. Scalable diffusion models with transformers. In *Proceedings of the IEEE/CVF international conference on computer vision*, pp. 4195–4205, 2023.

Kien T Pham, Jingye Chen, and Qifeng Chen. Tale: Training-free cross-domain image composition via adaptive latent manipulation and energy-guided optimization. In *Proceedings of the 32nd ACM International Conference on Multimedia*, pp. 3160–3169, 2024.

Trung X Pham, Zhang Kang, Ji Woo Hong, Xuran Zheng, and Chang D Yoo. E-md3c: Taming masked diffusion transformers for efficient zero-shot object customization. *arXiv preprint arXiv:2502.09164*, 2025.

Dustin Podell, Zion English, Kyle Lacey, Andreas Blattmann, Tim Dockhorn, Jonas Müller, Joe Penna, and Robin Rombach. SDXL: Improving latent diffusion models for high-resolution image synthesis. In *The Twelfth International Conference on Learning Representations*, 2024.

Ben Poole, Ajay Jain, Jonathan T Barron, and Ben Mildenhall. Dreamfusion: Text-to-3d using 2d diffusion. In *The Eleventh International Conference on Learning Representations*.

Yuandong Pu, Le Zhuo, Kaiwen Zhu, Liangbin Xie, Wenlong Zhang, Xiangyu Chen, Pneg Gao, Yu Qiao, Chao Dong, and Yihao Liu. Lumina-omnilv: A unified multimodal framework for general low-level vision. *arXiv preprint arXiv:2504.04903*, 2025.

Pengchong Qiao, Lei Shang, Chang Liu, Baigui Sun, Xiangyang Ji, and Jie Chen. Facechain-sude: Building derived class to inherit category attributes for one-shot subject-driven generation. In *Proceedings of the IEEE/CVF Conference on Computer Vision and Pattern Recognition*, pp. 7215–7224, 2024.

Zeju Qiu, Weiyang Liu, Haiwen Feng, Yuxuan Xue, Yao Feng, Zhen Liu, Dan Zhang, Adrian Weller, and Bernhard Schölkopf. Controlling text-to-image diffusion by orthogonal finetuning. *Advances in Neural Information Processing Systems*, 36:79320–79362, 2023.

Alec Radford, Jong Wook Kim, Chris Hallacy, Aditya Ramesh, Gabriel Goh, Sandhini Agarwal, Girish Sastry, Amanda Askell, Pamela Mishkin, Jack Clark, et al. Learning transferable visual models from natural language supervision. In *International conference on machine learning*, pp. 8748–8763. PMLR, 2021.

Nikhila Ravi, Valentin Gabeur, Yuan-Ting Hu, Ronghang Hu, Chaitanya Ryali, Tengyu Ma, Haitham Khedr, Roman Rädle, Chloe Rolland, Laura Gustafson, Eric Mintun, Junting Pan, Kalyan Vasudev Alwala, Nicolas Carion, Chao-Yuan Wu, Ross Girshick, Piotr Dollar, and Christoph Feichtenhofer. SAM 2: Segment anything in images and videos. In *The Thirteenth International Conference on Learning Representations*, 2025.

Nataniel Ruiz, Yuanzhen Li, Varun Jampani, Yael Pritch, Michael Rubinstein, and Kfir Aberman. Dreambooth: Fine tuning text-to-image diffusion models for subject-driven generation. In *Proceedings of the IEEE/CVF conference on computer vision and pattern recognition*, pp. 22500–22510, 2023.

Nataniel Ruiz, Yuanzhen Li, Neal Wadhwa, Yael Pritch, Michael Rubinstein, David E Jacobs, and Shlomi Fruchter. Magic insert: Style-aware drag-and-drop. In *Proceedings of the IEEE/CVF International Conference on Computer Vision*, pp. 15971–15981, 2025.

Patrick Schramowski, Manuel Brack, Björn Deiseroth, and Kristian Kersting. Safe latent diffusion: Mitigating inappropriate degeneration in diffusion models. In *Proceedings of the IEEE/CVF Conference on Computer Vision and Pattern Recognition*, pp. 22522–22531, 2023.

Shihao Shao and Qinghua Cui. 1st place solution in google universal images embedding. *arXiv preprint arXiv:2210.08473*, 2022.

Yichen Sheng, Jianming Zhang, and Bedrich Benes. Ssn: Soft shadow network for image compositing. In *Proceedings of the IEEE/CVF Conference on Computer Vision and Pattern Recognition*, pp. 4380–4390, 2021.

Jing Shi, Wei Xiong, Zhe Lin, and Hyun Joon Jung. Instantbooth: Personalized text-to-image generation without test-time finetuning. In *Proceedings of the IEEE/CVF Conference on Computer Vision and Pattern Recognition*, pp. 8543–8552, 2024a.

Yichun Shi, Peng Wang, and Weilin Huang. Seededit: Align image re-generation to image editing. *arXiv preprint arXiv:2411.06686*, 2024b.

Jiaming Song, Chenlin Meng, and Stefano Ermon. Denoising diffusion implicit models. *International Conference on Learning Representations*, 2021.

Wensong Song, Hong Jiang, Zongxing Yang, Ruijie Quan, and Yi Yang. Insert anything: Image insertion via in-context editing in dit. *arXiv preprint arXiv:2504.15009*, 2025a.

Yeji Song, Jimyeong Kim, Wonhark Park, Wonsik Shin, Wonjong Rhee, and Nojun Kwak. Harmonizing visual and textual embeddings for zero-shot text-to-image customization. In *Proceedings of the AAAI Conference on Artificial Intelligence*, volume 39, pp. 20549–20557, 2025b.

Yizhi Song, Zhifei Zhang, Zhe Lin, Scott Cohen, Brian Price, Jianming Zhang, Soo Ye Kim, and Daniel Aliaga. Objectstitch: Object compositing with diffusion model. In *Proceedings of the IEEE/CVF Conference on Computer Vision and Pattern Recognition*, pp. 18310–18319, 2023.

Yizhi Song, Zhifei Zhang, Zhe Lin, Scott Cohen, Brian Price, Jianming Zhang, Soo Ye Kim, He Zhang, Wei Xiong, and Daniel Aliaga. Imprint: Generative object compositing by learning identity-preserving representation. In *Proceedings of the IEEE/CVF Conference on Computer Vision and Pattern Recognition*, pp. 8048–8058, 2024.

Jiale Tao, Yanbing Zhang, Qixun Wang, Yiji Cheng, Haofan Wang, Xu Bai, Zhengguang Zhou, Ruihuang Li, Linqing Wang, Chunyu Wang, et al. Instantcharacter: Personalize any characters with a scalable diffusion transformer framework. *arXiv preprint arXiv:2504.12395*, 2025.

Gemma Canet Tarrés, Zhe Lin, Zhifei Zhang, He Zhang, Andrew Gilbert, John Collomosse, and Soo Ye Kim. Multitwine: Multi-object compositing with text and layout control. In *Proceedings of the Computer Vision and Pattern Recognition Conference*, pp. 8094–8104, 2025.

Yoad Tewel, Rinon Gal, Dvir Samuel, Yuval Atzmon, Lior Wolf, and Gal Chechik. Add-it: Training-free object insertion in images with pretrained diffusion models. In *The Thirteenth International Conference on Learning Representations*.

Shashank Tripathi, Siddhartha Chandra, Amit Agrawal, Ambrish Tyagi, James M Rehg, and Visesh Chari. Learning to generate synthetic data via compositing. In *Proceedings of the IEEE/CVF Conference on Computer Vision and Pattern Recognition*, pp. 461–470, 2019.

Haofan Wang, Matteo Spinelli, Qixun Wang, Xu Bai, Zekui Qin, and Anthony Chen. Instantstyle: Free lunch towards style-preserving in text-to-image generation. *arXiv preprint arXiv:2404.02733*, 2024a.

Haoxuan Wang, Jinlong Peng, Qingdong He, Hao Yang, Ying Jin, Jiafu Wu, Xiaobin Hu, Yanjie Pan, Zhenye Gan, Mingmin Chi, et al. Unicombine: Unified multi-conditional combination with diffusion transformer. *arXiv preprint arXiv:2503.09277*, 2025a.

Qian Wang, Biao Zhang, Michael Birsak, and Peter Wonka. Instructedit: Improving automatic masks for diffusion-based image editing with user instructions. *arXiv preprint arXiv:2305.18047*, 2023.

Qixun Wang, Xu Bai, Haofan Wang, Zekui Qin, Anthony Chen, Huaxia Li, Xu Tang, and Yao Hu. Instantid: Zero-shot identity-preserving generation in seconds. *arXiv preprint arXiv:2401.07519*, 2024b.

Yibin Wang, Weizhong Zhang, Jianwei Zheng, and Cheng Jin. Primecomposer: Faster progressively combined diffusion for image composition with attention steering. In *Proceedings of the 32nd ACM International Conference on Multimedia*, pp. 10824–10832, 2024c.

Yibin Wang, Zhimin Li, Yuhang Zang, Chunyu Wang, Qinglin Lu, Cheng Jin, and Jiaqi Wang. Unified multimodal chain-of-thought reward model through reinforcement fine-tuning. *arXiv preprint arXiv:2505.03318*, 2025b.

Yibin Wang, Yuhang Zang, Hao Li, Cheng Jin, and Jiaqi Wang. Unified reward model for multimodal understanding and generation. *arXiv preprint arXiv:2503.05236*, 2025c.

Zhou Wang, Alan C Bovik, Hamid R Sheikh, and Eero P Simoncelli. Image quality assessment: from error visibility to structural similarity. *IEEE transactions on image processing*, 13(4):600–612, 2004.

Yuxiang Wei, Yabo Zhang, Zhilong Ji, Jinfeng Bai, Lei Zhang, and Wangmeng Zuo. Elite: Encoding visual concepts into textual embeddings for customized text-to-image generation. In *Proceedings of the IEEE/CVF International Conference on Computer Vision*, pp. 15943–15953, 2023.

Daniel Winter, Asaf Shul, Matan Cohen, Dana Berman, Yael Pritch, Alex Rav-Acha, and Yedid Hoshen. Objectmate: A recurrence prior for object insertion and subject-driven generation. In *Proceedings of the IEEE/CVF International Conference on Computer Vision*, pp. 16281–16291, 2025.

Huikai Wu, Shuai Zheng, Junge Zhang, and Kaiqi Huang. Gp-gan: Towards realistic high-resolution image blending. In *Proceedings of the 27th ACM international conference on multimedia*, pp. 2487–2495, 2019.

Shitao Xiao, Yueze Wang, Junjie Zhou, Huaying Yuan, Xingrun Xing, Ruiran Yan, Chaofan Li, Shuting Wang, Tiejun Huang, and Zheng Liu. Omnigen: Unified image generation. In *Proceedings of the Computer Vision and Pattern Recognition Conference*, pp. 13294–13304, 2025.

Jiazheng Xu, Xiao Liu, Yuchen Wu, Yuxuan Tong, Qinkai Li, Ming Ding, Jie Tang, and Yuxiao Dong. Imagereward: Learning and evaluating human preferences for text-to-image generation. *Advances in Neural Information Processing Systems*, 36:15903–15935, 2023.

Jiazheng Xu, Yu Huang, Jiale Cheng, Yuanming Yang, Jiajun Xu, Yuan Wang, Wenbo Duan, Shen Yang, Qunlin Jin, Shurun Li, et al. Visionreward: Fine-grained multi-dimensional human preference learning for image and video generation. *arXiv preprint arXiv:2412.21059*, 2024.

Ben Xue, Shenghui Ran, Quan Chen, Rongfei Jia, Binqiang Zhao, and Xing Tang. Dccf: Deep comprehensible color filter learning framework for high-resolution image harmonization. In *European Conference on Computer Vision*, pp. 300–316. Springer, 2022.

Le Xue, Manli Shu, Anas Awadalla, Jun Wang, An Yan, Senthil Purushwalkam, Honglu Zhou, Viraj Prabhu, Yutong Dai, Michael S Ryoo, et al. xgen-mm (blip-3): A family of open large multimodal models. *arXiv preprint arXiv:2408.08872*, 2024.

Zexuan Yan, Yue Ma, Chang Zou, Wenteng Chen, Qifeng Chen, and Linfeng Zhang. Eedit: Rethinking the spatial and temporal redundancy for efficient image editing. *arXiv preprint arXiv:2503.10270*, 2025.

Binxin Yang, Shuyang Gu, Bo Zhang, Ting Zhang, Xuejin Chen, Xiaoyan Sun, Dong Chen, and Fang Wen. Paint by example: Exemplar-based image editing with diffusion models. In *Proceedings of the IEEE/CVF conference on computer vision and pattern recognition*, pp. 18381–18391, 2023.

Ling Yang, Zhaochen Yu, Chenlin Meng, Minkai Xu, Stefano Ermon, and Bin Cui. Mastering text-to-image diffusion: Recaptioning, planning, and generating with multimodal llms. In *Forty-first International Conference on Machine Learning*, 2024.

Hu Ye, Jun Zhang, Sibo Liu, Xiao Han, and Wei Yang. Ip-adapter: Text compatible image prompt adapter for text-to-image diffusion models. *arXiv preprint arXiv:2308.06721*, 2023.

Qifan Yu, Wei Chow, Zhongqi Yue, Kaihang Pan, Yang Wu, Xiaoyang Wan, Juncheng Li, Siliang Tang, Hanwang Zhang, and Yueting Zhuang. Anyedit: Mastering unified high-quality image editing for any idea. In *Proceedings of the Computer Vision and Pattern Recognition Conference*, pp. 26125–26135, 2025a.

Yongsheng Yu, Ziyun Zeng, Haitian Zheng, and Jiebo Luo. Omnipaint: Mastering object-oriented editing via disentangled insertion-removal inpainting. *arXiv preprint arXiv:2503.08677*, 2025b.

Bo Zhang, Yuxuan Duan, Jun Lan, Yan Hong, Huijia Zhu, Weiqiang Wang, and Li Niu. Controlcom: Controllable image composition using diffusion model. *arXiv preprint arXiv:2308.10040*, 2023a.

Kai Zhang, Lingbo Mo, Wenhu Chen, Huan Sun, and Yu Su. Magicbrush: A manually annotated dataset for instruction-guided image editing. *Advances in Neural Information Processing Systems*, 36:31428–31449, 2023b.

Lingzhi Zhang, Tarmily Wen, Jie Min, Jiancong Wang, David Han, and Jianbo Shi. Learning object placement by inpainting for compositional data augmentation. In *European Conference on Computer Vision*, pp. 566–581. Springer, 2020a.

Lingzhi Zhang, Tarmily Wen, and Jianbo Shi. Deep image blending. In *Proceedings of the IEEE/CVF Winter Conference on Applications of Computer Vision*, pp. 231–240, 2020b.

Richard Zhang, Phillip Isola, Alexei A Efros, Eli Shechtman, and Oliver Wang. The unreasonable effectiveness of deep features as a perceptual metric. In *Proceedings of the IEEE conference on computer vision and pattern recognition*, pp. 586–595, 2018.

Shuyang Zhang, Runze Liang, and Miao Wang. Shadowgan: Shadow synthesis for virtual objects with conditional adversarial networks. *Computational Visual Media*, 5(1):105–115, 2019.

Zechuan Zhang, Ji Xie, Yu Lu, Zongxin Yang, and Yi Yang. In-context edit: Enabling instructional image editing with in-context generation in large scale diffusion transformer. *arXiv preprint arXiv:2504.20690*, 2025.

Haozhe Zhao, Xiaojian Shawn Ma, Liang Chen, Shuzheng Si, Rujie Wu, Kaikai An, Peiyu Yu, Minjia Zhang, Qing Li, and Baobao Chang. Ultraedit: Instruction-based fine-grained image editing at scale. *Advances in Neural Information Processing Systems*, 37:3058–3093, 2024.

Kaiwen Zheng, Cheng Lu, Jianfei Chen, and Jun Zhu. Improved techniques for maximum likelihood estimation for diffusion odes. In *International Conference on Machine Learning*, pp. 42363–42389. PMLR, 2023.

Junhao Zhuang, Yanhong Zeng, Wenran Liu, Chun Yuan, and Kai Chen. A task is worth one word: Learning with task prompts for high-quality versatile image inpainting. In *European Conference on Computer Vision*, pp. 195–211. Springer, 2024.

Appendix

Table of Contents

A Related Work

A.1 Image Composition

Image composition involves integrating specific objects and scenarios from user-provided photos, often guided by text prompts. Traditionally, this process is divided into sub-tasks (Niu et al., 2021), including object placement (Azadi et al., 2020; Chen & Kae, 2019; Lin et al., 2018; Tripathi et al., 2019; Zhang et al., 2020a), image blending (Wu et al., 2019; Zhang et al., 2020b), image harmonization (Cao et al., 2023; Lu et al., 2023b; Zhang et al., 2020b; Cong et al., 2020; Cun & Pun, 2020; Jiang et al., 2021; Xue et al., 2022), and shadow generation (Hong et al., 2022; Liu et al., 2020; Sheng et al., 2021; Zhang et al., 2019), each typically handled by distinct models and pipelines. However, with the rise of diffusion-based generative models, recent approaches have shifted toward unified frameworks that address all sub-tasks simultaneously. These methods are broadly classified into training-based and training-free approaches.

Training-based methods fine-tune foundational models using datasets tailored for image composition. Early methods like Paint by Example (Yang et al., 2023) and ObjectStitch (Song et al., 2023) use CLIP to encode subject features, ensuring high semantic similarity between inserted objects and reference images. These approaches use image augmentation to create training datasets, enabling effective training. GLIGEN (Li et al., 2023c) incorporates grounding information into new trainable layers of a pre-trained diffusion model via a gated mechanism. ControlCom (Zhang et al., 2023a) integrates 2-dim indicator vector to improve controllability. DreamCom (Lu et al., 2023c) and MureObjectStitch (Chen et al., 2024a) fine-tune models with small sets of reference images to preserve subject identity. AnyDoor (Chen et al., 2024c), IMPRINT (Song et al., 2024), and E-MD3C (Pham et al., 2025) leverage DINOv2 to enhance identity fidelity and control over shape and pose, drawing supervision from video data. MimicBrush (Chen et al., 2024b) similarly uses video-derived supervision for imitative editing. In contrast, MADD (He et al., 2024), ObjectMate (Winter et al., 2025), and OmniPaint (Yu et al., 2025b) employ image inpainting models to generate higher-quality training datasets compared to those based on image or video augmentation. Multitwine (Tarrés et al., 2025) enables the integration of multiple objects, capturing interactions from simple positional relationships to complex actions requiring reposing. DreamFuse (Huang et al., 2025) uses a Positional Affine mechanism to embed foreground size and position into the background, fostering effective foreground-background interaction through shared attention. Insert Anything (Song et al., 2025a) and UniCombine (Wang et al., 2025a) introduces a FLUX-based, multi-conditional generative framework that handles diverse condition combinations. However, these methods often bias the generative priors of base models toward curated datasets, resulting in unnatural compositions, such as implausible object-environment interactions (e.g., missing or unrealistic shadows and reflections). This stems from the absence of a large-scale, high-quality, multi-resolution, real-world triplet dataset comprising an object, a scene, and the object seamlessly integrated into the scene, which is expensive to produce.

Training-free methods, on the other hand, modify the inference process of pre-trained models to achieve composition without additional training. Early approaches like TF-ICON (Lu et al., 2023d) leverage accurate image inversion to lay the groundwork for composition, achieved through composite self-attention map injection. TALE (Pham et al., 2024) and PrimeComposer (Wang et al., 2024c) build on TF-ICON to enhance identity preservation and background-object style adaptation. TIGIC (Li et al., 2024b) focuses on preserving non-target areas during composition. Thinking Outside the BBox (Canet Tarrés et al., 2024) enables unconstrained image compositing, unbound by input masks. FreeCompose (Chen et al., 2024e) employs a pipeline of object removal, image harmonization, and semantic composition. DreamEdit (Li et al., 2023b), UniCanvas (Jin et al., 2025), and Magic Insert (Ruiz et al., 2025) use test-time tuning to fine-tune models during inference. Addit (Tewel et al.) enables text-guided object insertion on FLUX, where users describe objects via text prompts instead of reference images. EEdit (Yan et al., 2025) recently improves TF-ICON on FLUX, introducing step-skipping to reduce time costs and spatial locality caching to minimize redundancy. However, training-free methods rely on precise image inversion and fragile attention surgery, which can lock inserted objects into the exact pose of the reference image, leading to awkward or contextually inappropriate orientations. Attention manipulation often causes instability and hyperparameter sensitivity, as feature or attention map injection does not always preserve subject identity. This creates a trade-off: stronger injection preserves identity but results in unnatural poses, while lighter injection yields more natural poses but compromises identity.

A.2 General Image Editing

Instruction-based image editing has evolved rapidly. Early systems relied on modular, two-stage pipelines: a multimodal language model first produced textual prompts, spatial guidance, or synthetic instruction–image pairs, and a separate diffusion model then executed the edit—as in InstructEdit (Wang et al., 2023), InstructPix2Pix (Brooks et al., 2023), MagicBrush (Zhang et al., 2023b), and BrushEdit (Li et al., 2024c). Recent work has shifted toward tightly integrated, instruction-centric architectures. Models such as SmartEdit (Huang et al., 2024), X2I (Ma et al., 2025a), RPG (Yang et al., 2024), AnyEdit (Yu et al., 2025a), and UltraEdit (Zhao et al., 2024) embed routing, task-aware objectives, and fine-grained controls directly into the network, yielding higher fidelity and more precise manipulation.

Unified generation-and-editing frameworks (e.g., OmniGen (Xiao et al., 2025), ACE (Han et al.), ACE++ (Mao et al., 2025), Lumina-OmniLV (Pu et al., 2025), Qwen2VL-Flux (Lu, 2024), DreamEngine (Chen et al., 2025), MetaQueries (Pan et al., 2025), Hidream-E1 (HiDream-ai, 2025)) treat editing as one capability of an end-to-end vision-language model, often fusing language embeddings with diffusion latents to provide context-aware, pixel-level control. Efficiency has advanced in parallel: ICEdit (Zhang et al., 2025) couples LoRA with mixture-of-experts tuning and optimized noise initialization, while SuperEdit (Ming et al., 2025) relies on higher-quality data and contrastive supervision to sustain performance at lower cost. Looking ahead, large foundation models such as Gemini (Gemini2.5, 2025) and GPT-5 (OpenAI, 2025) already show strong visual reasoning and coherent, instruction-guided image generation. Yet, despite extensive multimodal pre-training, they still fall short on image composition: object placement remains hard to control, lighting is often inconsistent, and subjects can drift in identity.

A.3 Subject-Driven Generation

Extensive research has explored subject-driven image generation, in which the output must not only portray the contexts described by the text prompt but also faithfully include the specific subject supplied by reference images. Methods in this area are divided into two categories—test-time fine-tuning customization and zero-shot customization—according to whether extra training is needed for each new subject. **Our framework accommodates both categories, so we provide two corresponding variants in the main paper.**

Test-time fine-tuning methods (Gal et al., 2022; Ruiz et al., 2023) adapt a pre-trained T2I model to a small set of reference images (typically 3 to 5 images). Although this step adds computational cost and latency, it offers the greatest flexibility for diverse customization requirements. Such methods are commonly grouped into three subclasses: data regularization, weight regularization, and loss regularization. In the data-regularization family, DreamBooth (Ruiz et al., 2023) limits overfitting by generating superclass images with the base T2I model and training on both reference and regularization images; Custom Diffusion (Kumari et al., 2023) improves regularization quality by retrieving real images; and Specialist Diffusion (Lu et al., 2023a) applies extensive data augmentation. Weight-regularization approaches (Gal et al., 2022; Hu et al.; Han et al., 2023; Qiu et al., 2023) confine updates to carefully chosen parameters, such as the subject-specific text embeddings or the singular values of weight matrices. Loss-regularization approaches, including Specialist Diffusion (Lu et al., 2023a), MagiCapture (Hyung et al., 2024), and FaceChain-SuDe (Qiao et al., 2024), introduce objective terms that respectively maximize CLIP-space similarity between generated and reference images, disentangle identity and style via masked facial reconstruction, or encourage correct superclass classification.

Zero-shot image customization methods avoid subject-specific fine-tuning at inference time but rely on extensive pre-training. For general subject customization, InstantBooth (Shi et al., 2024a) adds a visual encoder that captures coarse-to-fine image features from the references; BLIP-Diffusion (Li et al., 2024a) fine-tunes BLIP-2 (Li et al., 2023a) to extract multimodal subject representations; ELITE (Wei et al., 2023) maps reference images into hierarchical textual tokens through global and local networks; and Song et al. (Song et al., 2025b) enhance textual control by removing the projection of visual embeddings onto textual embeddings. For facial customization, InstantID (Wang et al., 2024b) isolates facial regions from reference images to extract appearance and structural cues. For style customization, InstantStyle (Wang et al., 2024a) identifies style-controlling layers and injects IP-Adapter features (Ye et al., 2023) into those layers to achieve style transfer. In-

stantCharacter (Tao et al., 2025), IP-Adapter (Ye et al., 2023), and PuLID (Guo et al., 2024) have each released versions compatible with the FLUX model.

B Visualizing the Impact of Adaptive Background Blending

Although our loss function aims to find a new latent within the manifold learned by the adapter, encouraging the adapter-augmented T2I model's predictions to closely match those of the base model on the original noisy latent, this early-stage optimization primarily preserves structural elements rather than fine details. Consequently, discrepancies in fine-grained features often arise between the masked and unmasked regions. As illustrated in Fig. 9, we compare the composite images generated using our Adaptive Background Blending (ABB) method with those produced via direct background blending using the rectangular user mask. For clarity, we enlarge the boundary areas of each image (highlighted in pink dashed boxes) to better reveal differences.

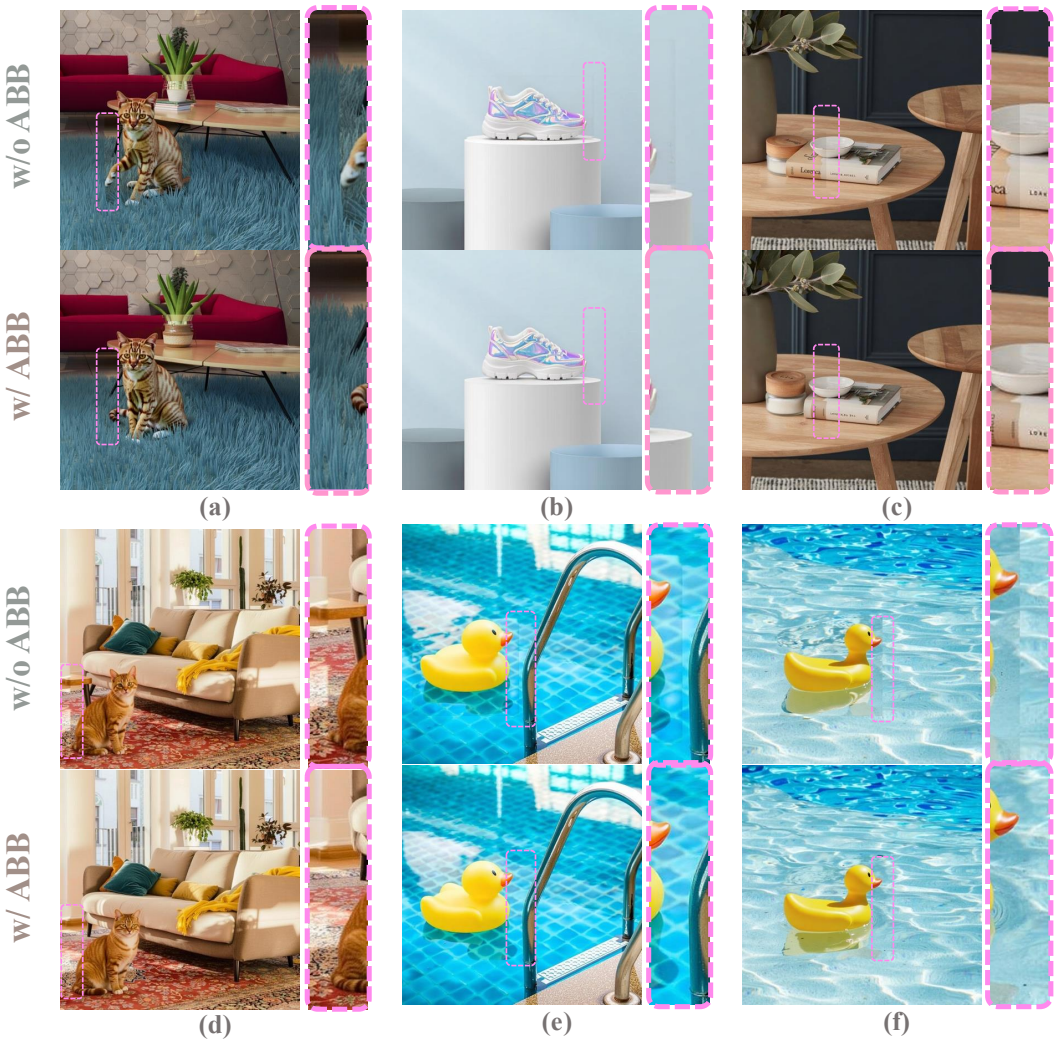

Figure 9: Comparison of composites from our Adaptive Background Blending (ABB) method and direct blending with a rectangular mask. Boundary regions within pink dashed boxes are enlarged for clarity. Please zoom in to see details.

C Equivalence of Query Blurring and Attention Weight Blurring

Consider a 2D Gaussian filter $\boldsymbol{G}$ applied as a convolution operation, denoted by $\circledast$. The self-attention weights are computed as $\boldsymbol{Q}\boldsymbol{K}^\top$, where $\boldsymbol{Q}, \boldsymbol{K} \in \mathbb{R}^{n\times d}$, with n being the sequence length and d the embedding dimension. We explore the effect of applying a Gaussian blur to the attention weights and its equivalence to blurring the query matrix.

C.1 Blurring the Query Matrix

Blurring the self-attention weights $\boldsymbol{Q}\boldsymbol{K}^\top$ with a 2D Gaussian filter $\boldsymbol{G}$ can be expressed as:

$$\boldsymbol{G} \circledast (\boldsymbol{Q}\boldsymbol{K}^\top), \tag{6}$$

where $\circledast$ denotes 2D convolution. Due to the linearity of convolution, there exists a Toeplitz matrix $\boldsymbol{B} \in \mathbb{R}^{n\times n}$ such that the convolution operation can be represented as a matrix multiplication:

$$\boldsymbol{G} \circledast (\boldsymbol{Q}\boldsymbol{K}^\top) = \boldsymbol{B}(\boldsymbol{Q}\boldsymbol{K}^\top). \tag{7}$$

Using the properties of matrix multiplication, we can rewrite this as:

$$\boldsymbol{B}(\boldsymbol{Q}\boldsymbol{K}^\top) = (\boldsymbol{B}\boldsymbol{Q})\boldsymbol{K}^\top. \tag{8}$$

Since the convolution operation is linear, applying the Gaussian filter $\boldsymbol{G}$ to the rows of $\boldsymbol{Q}$ yields:

$$\boldsymbol{B}\boldsymbol{Q} = \boldsymbol{G} \circledast \boldsymbol{Q}. \tag{9}$$

Thus, we obtain:

$$\boldsymbol{G} \circledast (\boldsymbol{Q}\boldsymbol{K}^\top) = (\boldsymbol{G} \circledast \boldsymbol{Q})\boldsymbol{K}^\top. \tag{10}$$

This establishes that blurring the query matrix $\boldsymbol{Q}$ with $\boldsymbol{G}$ is mathematically equivalent to applying the same blur to the self-attention weights $\boldsymbol{Q}\boldsymbol{K}^\top$. This equivalence suggests that query blurring can be used as a computationally efficient proxy for smoothing attention weights, potentially reducing the need for direct manipulation of the attention matrix.

C.2 Blurring the Key and Value Matrices

In contrast, applying the Gaussian blur to the key matrix K does not yield a similar equivalence. Consider the convolution applied to K. The resulting attention weights become:

$$\boldsymbol{Q}(\boldsymbol{G} \circledast \boldsymbol{K})^\top = \boldsymbol{Q}(\boldsymbol{B}\boldsymbol{K})^\top = \boldsymbol{Q}\boldsymbol{K}^\top\boldsymbol{B}^\top. \tag{11}$$

Since $\boldsymbol{B}^\top \neq \boldsymbol{B}$ for a general Toeplitz matrix derived from a Gaussian filter, we have:

$$\boldsymbol{Q}\boldsymbol{K}^\top\boldsymbol{B}^\top \neq \boldsymbol{B}(\boldsymbol{Q}\boldsymbol{K}^\top). \tag{12}$$

Thus, blurring the key matrix $\boldsymbol{K}$ does not produce an equivalent effect to blurring the attention weights $\boldsymbol{Q}\boldsymbol{K}^\top$. A similar argument applies to the value matrix $\boldsymbol{V}$, as the output of self-attention, $(\boldsymbol{Q}\boldsymbol{K}^\top)\boldsymbol{V}$, involves $\boldsymbol{V}$ in a post-multiplication step, and convolution on $\boldsymbol{V}$ does not commute with the attention weight computation in the same manner.

C.3 Implementation Details of Gaussian Blurring

For the 2D Gaussian filtering step, we adopt the implementation provided by the `kornia` library. Following standard engineering practice, we set the kernel radius to $r = 3\sigma$, since three standard deviations capture approximately 99.7% of the Gaussian mass. Consequently, the kernel size is chosen as the nearest odd integer to $2r = 6\sigma$. In all of our experiments we use $\sigma = 10$ (see Tab. 5).

The procedure is applied to query embeddings by reshaping them into spatial feature maps, performing Gaussian smoothing, and then mapping them back into the sequence domain prior to attention computation. The full workflow is given below:

Algorithm 2 Implementation Details of 2D Gaussian Blurring

Input: A query matrix $\mathbf{Q} \in \mathbb{R}^{B\times L\times D}$, key $\mathbf{K}$, value $\mathbf{V}$, spatial dimensions (H, W), Gaussian standard deviation σ.
Output: Attention output $\mathbf{O}$.

// Reshape query into spatial tensor
$\mathbf{Q}_{\text{sp}} \leftarrow \text{Reshape}(\mathbf{Q},\ (B, H, W, D))$
$\mathbf{Q}_{\text{sp}} \leftarrow \text{Permute}(\mathbf{Q}_{\text{sp}},\ (0, 3, 1, 2))$ ▷ $B \times D \times H \times W$
// Construct Gaussian kernel size
$k \leftarrow 6\sigma$
$k \leftarrow k - (k \bmod 2) + 1$ ▷ Ensure odd kernel size
$\text{kernel\_size} \leftarrow (k, k)$
$\boldsymbol{\sigma} \leftarrow (\sigma, \sigma)$
// Apply 2D Gaussian smoothing
$\mathbf{Q}_{\text{sp}} \leftarrow \text{kornia.filters.gaussian\_blur2d}(\mathbf{Q}_{\text{sp}},\ \text{kernel\_size},\ \boldsymbol{\sigma})$
// Reshape smoothed queries back to sequence form
$\mathbf{Q}' \leftarrow \text{Permute}(\mathbf{Q}_{\text{sp}},\ (0, 2, 3, 1))$
$\mathbf{Q}' \leftarrow \text{Reshape}(\mathbf{Q}',\ (B, L, D))$
// Compute attention
$\mathbf{A} \leftarrow \text{softmax}\left(\frac{\mathbf{Q}'\mathbf{K}^\top}{\sqrt{D}}\right)$
$\mathbf{O} \leftarrow \mathbf{AV}$
return $\mathbf{O}$

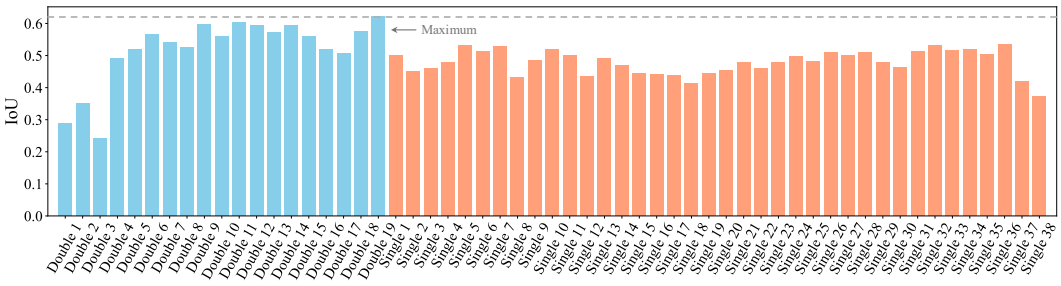

Figure 10: The IoU is calculated between the mask produced from each block and the ground-truth mask, which is obtained by segmenting the final generated images using SAM. The IoU for each block is averaged over 100 images.

D Evaluating Cross-Attention Map Accuracy via IoU

To identify the most accurate cross-attention maps that reflect the location of the generated object, we first create 100 prompts containing a main subject (e.g.,"a dog is sleeping on a couch") using GPT-5. These prompts are then used to generate 100 images with FLUX.1-dev, employing 20 denoising steps. Cross-attention maps are extracted from 19 multi-stream (or double-stream) blocks and 38 single-stream blocks across all denoising steps. The maps are averaged over the 20 steps and subsequently normalized and binarized, resulting in a total of 57 binary masks.

To determine which of these 57 masks is the most accurate, we compute the Intersection over Union (IoU) between each mask and a ground-truth mask obtained by segmenting the final generated images using SAM (Ravi et al., 2025). The IoU for each block is averaged over the 100 generated images. The results are presented in Fig. 10, showing that the cross-attention maps from the last multi-stream (or double-stream) block achieve the highest segmentation accuracy. A visualization of the cross-attention maps from all blocks is provided in Fig. 11.

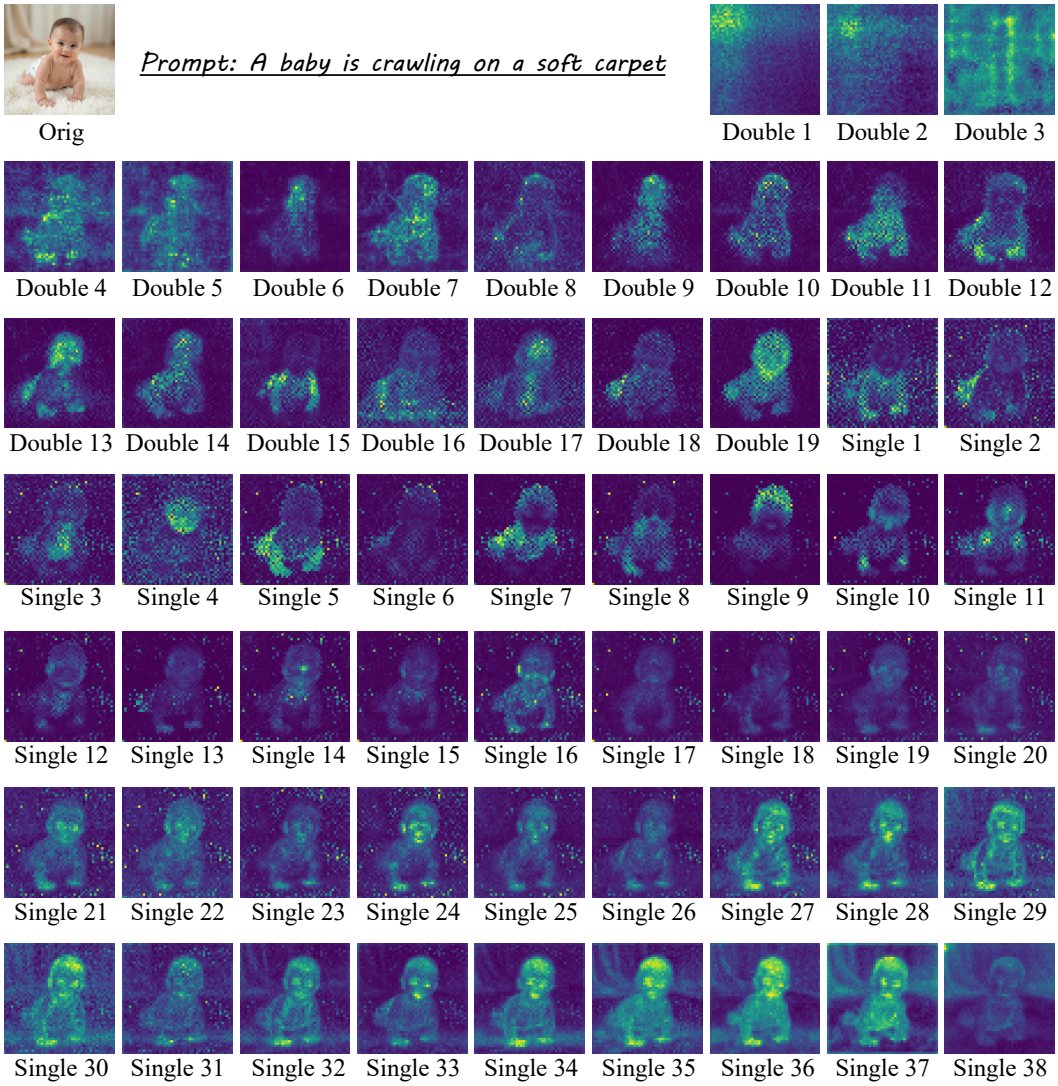

Figure 11: Visualization of cross-attention maps from different MMDiT blocks of FLUX.1-dev.

E Experiments with SDXL, SD3.5, and PixArt

Our framework introduces a novel, model-agnostic approach for enhancing generative architectures, anchored by three synergistic components: Manifold-Steered Anchor (MSA) loss, Degradation-Suppression Guidance (DSG), and Adaptive Background Blending (ABB). These components are meticulously designed to leverage ubiquitous features of modern generative models, ensuring seamless integration without requiring architectural modifications. Specifically, MSA utilizes either LoRA-based personalization or a pretrained personalization adapter, DSG capitalizes on widely available self-attention maps, and ABB harnesses text–image cross-attention maps, a staple in most text-to-image pipelines. This design ensures broad applicability across diverse generative models.

In the main text, we showcase the effectiveness of our approach on Flux, a leading open-source model. To establish its generalizability, we conduct experiments on SDXL (Podell et al., 2024), SD3.5 (Esser et al., 2024), and PixArt (Chen et al.) across DreamEditBench and ComplexCompo. The results are presented in Tab. 3. On DreamEditBench, our LoRA-based variant with Flux achieves state-of-the-art performance in subject identity preservation, while delivering superior image quality. Similarly, on ComplexCompo, the Flux-LoRA configuration excels in identity consistency and image fidelity. Notably, the framework's benefits extend beyond a single model family: both SDXL and

PixArt-Σ exhibit substantial performance gains, affirming the approach's generality and adaptability across diverse generative architectures.

Table 3: Comparison of compositional performance across two benchmarks with **different base models**. The best result in each column is highlighted in **bold**, while the second-best is underlined. Metrics shown in pink are those specifically trained to better align with human preferences. Abbreviations: IRF: Instance Retrieval Features; IR = ImageReward; VR = VisionReward.

Bench	Method	Base Model	Subject Identity Consistency				Background		Image Quality	
			CLIP-I ↑	DINOv2 ↑	IRF ↑	DreamSim ↓	LPIPS ↓	SSIM ↑	IR ↑	VR ↑
DreamEdit-Bench (220)	Flux.1 Fill	FLUX	0.7328	0.6745	0.5754	0.5233	0.0166	0.9076	0.5577	3.5997
	Ours-Adapter	SDXL	0.7944	0.7334	0.7659	0.3761	0.0238	0.8922	0.5621	3.6158
	Ours-Adapter	SD3.5	0.8054	0.7407	0.7699	0.3745	**0.0234**	0.8937	0.5701	3.6187
	Ours-LoRA	PixArt-Σ	0.8098	0.7445	0.7798	0.3612	0.0251	0.8875	0.5842	3.6198
	Ours-Adapter	FLUX	0.8086	0.7415	0.7702	0.3730	0.0236	**0.8959**	0.5709	**3.6234**
	Ours-LoRA	FLUX	**0.8125**	**0.7452**	**0.7900**	**0.3577**	0.0271	0.8847	**0.5906**	3.6161
Complex-Compo (300)	Flux.1 Fill	FLUX	0.7108	0.6475	0.5466	0.6018	0.0232	0.7442	0.4088	3.5737
	Ours-Adapter	SDXL	0.7657	0.7084	0.6862	0.4457	0.0457	0.7612	0.3894	3.5987
	Ours-Adapter	SD3.5	0.7701	0.7091	0.6977	0.4173	**0.0401**	0.7784	0.4091	**3.6021**
	Ours-LoRA	PixArt-Σ	0.7924	0.7287	0.7311	0.3603	0.0424	0.7698	**0.4277**	3.5988
	Ours-Adapter	FLUX	0.7721	0.7107	0.6764	0.4294	0.0404	**0.7789**	0.4090	3.6020
	Ours-LoRA	FLUX	**0.7999**	**0.7384**	**0.7659**	**0.3542**	0.0430	0.7634	0.4246	3.5951

F User Study

We conduct a user study involving 50 participants. Each participant was asked to complete 50 ranking tasks. In each task, they were shown 13 composition results generated by different methods, along with a reference subject image.

To ensure a balanced evaluation, 25 of the tasks were randomly sampled from DreamEditBench and the remaining 25 from ComplexCompo. Participants were asked to rank the results based on two key criteria: (1) subject identity consistency and (2) composition realism. A lower rank (e.g., 1st) indicates a better composition result, while a higher rank (e.g., 13th) reflects a less favorable outcome.

We summarize the average ranking scores for each method in Tab. 4. Our method received the most favorable rankings from the majority of participants, demonstrating its effectiveness in producing high-quality compositions.

G Benchmark Details

Our benchmark consists of 300 triplets, each comprising a subject image, a background image, and a bounding box. The subject images are identical to those used in DreamEditBench (Li et al., 2023b; Ruiz et al., 2023), while the background images are sampled from the OpenImages dataset (Kuznetsova et al., 2020). These backgrounds exhibit a variety of aspect ratios and resolutions, including landscape and portrait formats, such as 768×1088, 768×1072, 768×1024, 768×1152, 1024×768, 1152×768, 1200×768, 848×768, and 1360×768. The bounding boxes are manually designed to ensure that the size and placement of the inserted subjects are contextually appropriate and visually plausible. The benchmark will be released publicly.

Table 4: Average ranking scores from the user study on image composition methods. Lower is better.

Method	Training-Free	Average Ranking (Lower is Better)
MADD	✘	12.44
ObjectStitch	✘	11.80
DreamCom	✘	6.66
AnyDoor	✘	4.12
UniCombine	✘	2.94
PBE	✘	4.94
TIGIC	✔	9.74
TALE	✔	9.06
TF-ICON	✔	8.36
DreamEdit	✔	6.36
EEdit	✔	10.76
Ours-Adapter	✔	2.30
Ours-LoRA	✔	**1.52**

H Prompts for Proprietary Foundation Models

To perform image composition with proprietary, general-purpose multimodal foundation models (e.g., GPT-5 (OpenAI, 2025), Gemini 2.5 Pro (Gemini2.5, 2025), SeedEdit/Doubao (Shi et al., 2024b), and Grok 4 (gro, 2025)), we upload three images: (1) Subject image; (2) Background image; and (3) Mask image defining the insertion region.

We then issue a prompt of the following form (with the resolution and coordinates adjusted for each case):

> *Please insert the object from the first uploaded image into the second image. The target region for insertion is defined by the mask in the third image. For reference, the resolution of the second image is* 1152×768*, and the bounding box for placement is specified by the top-left and bottom-right coordinates:* $(x_1 = 550, y_1 = 600, x_2 = 700, y_2 = 750)$*. The inserted object should retain the same identity and appearance as in the first image. The final composite should appear realistic, natural, and physically plausible.*

I Subject Identity Metrics Analysis

In our experiments we found that widely-used subject-identity metrics such as CLIP-I (Radford et al., 2021) and DINOv2 (Oquab et al., 2024) correlate poorly with human preferences. Because they focus almost exclusively on semantic similarity, they ignore appearance changes introduced by lighting, shadows, reflections, and surrounding context. Fig. 12(b) presents several image pairs produced by AnyDoor (left) and by our method (right); the corresponding CLIP-I (↑) (Radford et al., 2021), DINOv2 (↑) (Oquab et al., 2024), IRF (↑) (Shao & Cui, 2022), and DreamSim (↓) (Fu et al., 2023) scores are shown beneath each image, with the better score highlighted in red. Although the AnyDoor results are visibly less realistic and less consistent, they nevertheless receive higher CLIP-I and DINOv2 scores, and in most cases higher IRF scores, demonstrating that these measures do not faithfully capture compositional quality.

A reliable metric should recognise the same object whether it is underwater (see Fig. 12(b)[(8), (17), (20)]), in shadow (see Fig. 12(b)[(9), (13), (19)]), partially occluded (see Fig. 12(b)[(2)]), or situated in a low-light or back-lit scene (see Fig. 12(b)[(5), (14), (15), (16)]). Among the metrics we evaluated, only DreamSim, which was designed to align more closely with human perception, consistently exhibits this desired behaviour.

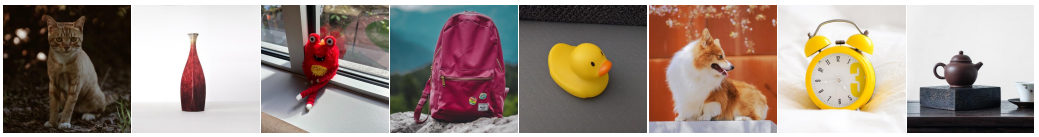

(a) Subject images used for evaluating identity consistency

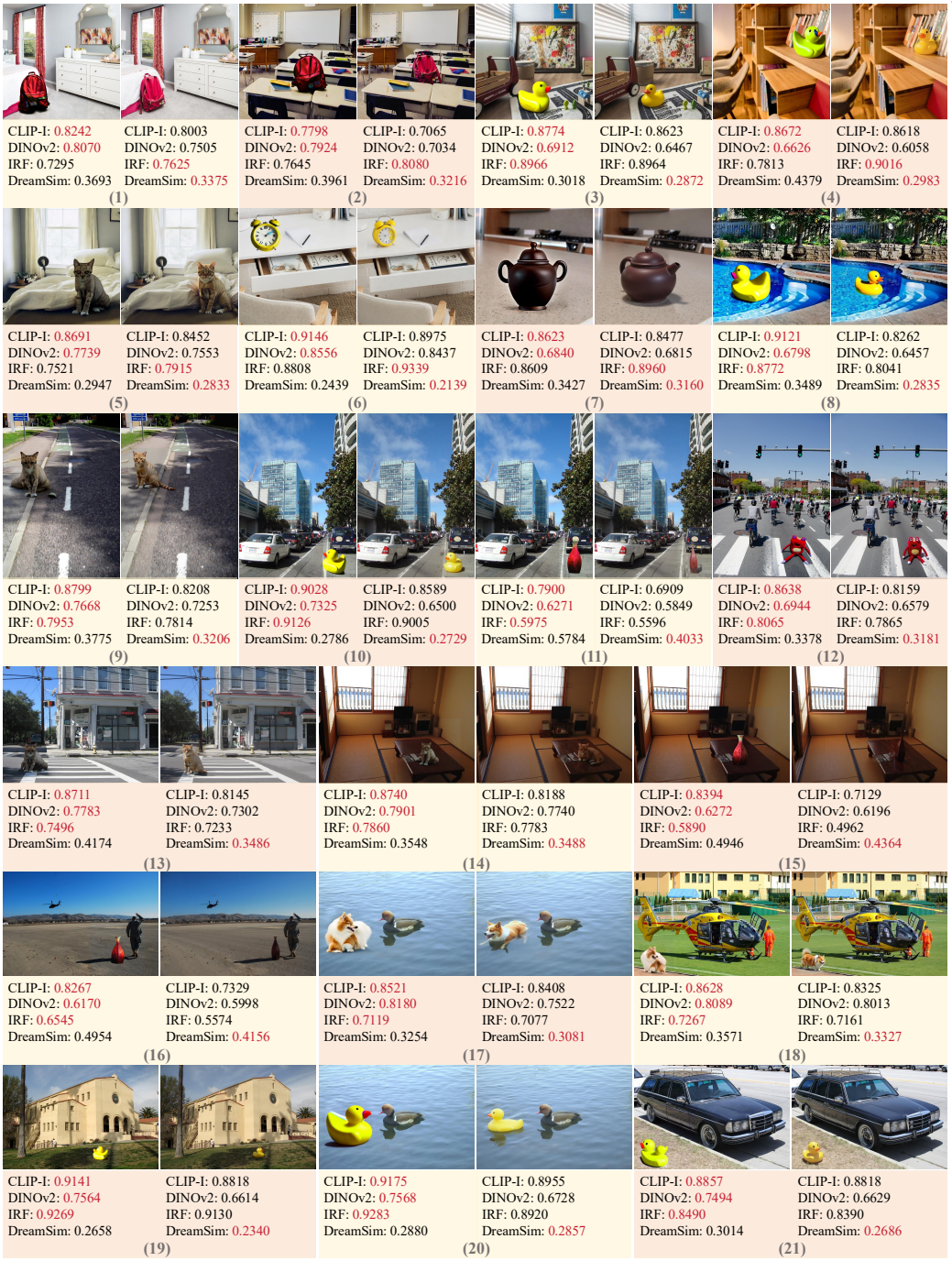

(b) Comparison of Identity Consistency Metrics

Figure 12: Comparison of Subject Identity Metrics. (a) Reference subject images used for metric calculations. (b) Image pairs generated by AnyDoor (left) and our method (right), with corresponding CLIP-I (↑), DINOv2 (↑), IRF (↑), and DreamSim (↓) scores displayed below each image; the better score is highlighted in red. Despite AnyDoor's results appearing less realistic and consistent, they often achieve higher CLIP-I, DINOv2, and IRF scores, indicating that these metrics may not reliably reflect compositional quality. In contrast, DreamSim provides a more reliable assessment.

Table 5: Hyperparameters of Our Frameworks. Bin Thresh = Binarization Threshold; #iter = Number of Iterations.

Variant	Denoising Setup		Manifold-Steered Anchor Loss			Degradation-Suppression Guidance			Adaptive Background Blending		
	Total steps $(T-1) \to 0$	Start step t_1	Step Range $t_1 \to \tau$	Learning Rate α	#iters k	Step Range $t_1 \to 0$	Scale η	Blur σ	Step Range $(t_1-1) \to 1$	Bin Thresh	Dilation Kernel Size
Ours-Adapter	$19 \to 0$	14	$14 \to 12$	500, 750, 1000	10	$14 \to 0$	0.5	10	$13 \to 1$	0.2	3
Ours-LoRA	$19 \to 0$	13	$13 \to 12$	50, 300	2	$13 \to 0$	0.7	10	$12 \to 1$	0.4	3

J Implementation Details

The hyperparameters used in our frameworks are summarized in Tab. 5. Under Denoising Setup, "Total steps" refers to the full diffusion/noising schedule, which specifies a sequence of 20 values of σ_t across timesteps t. However, our method does not begin denoising at the first timestep. As shown in Algorithm 1, it starts at $t_1 = 14$ (Ours-Adapter), resulting in 15 denoising steps in total. Under MSA loss, "Step Range" indicates the subset of denoising steps to which MSA optimization is applied. For the adapter setting, the MSA loss is applied only to the first three denoising steps (from $t = 14$ to $t = 12$). In addition, since a LoRA is trained for a specific subject, it provides a more tailored prior than the generic adapter, allowing it to converge in fewer steps and with lower overall compute.

Each baseline is implemented according to the configuration settings recommended in its original publication. The repositories utilized for each baseline are listed below:

1. MADD: https://github.com/KaKituken/affordance-aware-any
2. ObjectStitch: https://github.com/bcmi/ObjectStitch-Image-Composition
3. DreamCom: https://github.com/bcmi/DreamCom-Image-Composition
4. AnyDoor: https://github.com/ali-vilab/AnyDoor
5. UniCombine: https://github.com/Xuan-World/UniCombine
6. PBE: https://github.com/Fantasy-Studio/Paint-by-Example
7. TIGIC: https://github.com/zrealli/TIGIC
8. TALE: https://github.com/tkpham3105/TALE
9. TF-ICON: https://github.com/Shilin-LU/TF-ICON
10. DreamEdit: https://github.com/DreamEditBenchTeam/DreamEdit
11. EEdit: https://github.com/yuriYanZeXuan/EEdit

K Discussion on Inversion vs. One-Step Forward Diffusion

We provide an expanded discussion of our design choice between inversion and one-step forward diffusion to better clarify the motivation behind our approach. In training-free image editing, both inversion and one-step forward diffusion are commonly used to obtain a noisy latent that serves as the starting point for subsequent optimization or denoising. In our framework, we intentionally adopt one-step forward diffusion as a practical substitute for inversion. Our method does not depend on the initial latent to preserve object identity. Instead, the MSA loss extracts object-specific information from the adapter/LoRA and injects it into the latent during the editing process.

This design choice is motivated by a practical observation: many modern models are distilled for speed, making accurate inversion difficult to achieve in practice. When inversion cannot reliably encode object identity, its benefit becomes limited. In such cases, a noisy latent that still retains enough background structure is sufficient as a starting point. For this reason, we adopt one-step forward diffusion as a pragmatic replacement for inversion, rather than a theoretically equivalent alternative. It offers two advantages: (i) it avoids the accuracy limitations of inversion on distilled models, making it more broadly applicable, and (ii) it is faster than performing an inversion.

Table 6: Image Quality Evaluation Results using HPSv3 and UnifiedReward variants.

Bench	Method	HPSv3	UnifiedReward-2.0-qwen3vl-8b					UnifiedReward-Edit-qwen3vl-8b					UnifiedReward-Think-qwen-7b				
			Instruction		Quality		Average	Instruction		Quality		Average	Instruction		Quality		Average
			Success	Overedit	Natural	Artifact		Success	Overedit	Natural	Artifact		Success	Overedit	Natural	Artifact	
Dream-Edit-Bench (220)	MADD (He et al., 2024)	1.2443	14.2273	12.3727	16.6153	18.6807	15.4740	11.8091	17.8727	13.1045	12.4727	13.8148	14.7553	16.2128	19.1103	20.5724	17.6627
	ObjectStitch (Song et al., 2023)	7.4529	19.9954	16.8721	21.0455	21.8864	19.9499	16.2500	21.2000	18.6545	20.6500	19.1886	20.7500	17.7614	21.0563	20.7676	20.0838
	DreamCom (Lu et al., 2023c)	5.9324	18.1818	15.4818	23.5388	**24.0502**	20.3132	14.0727	22.5409	21.0091	22.0955	19.9296	18.5263	15.4737	21.6641	21.6953	19.3399
	AnyDoor (Chen et al., 2024c)	8.4867	23.2146	**17.8128**	20.9772	21.9361	20.9852	19.0909	20.6000	17.4182	19.2864	19.0989	21.2083	18.5694	21.9214	21.5929	20.8230
	UniCombine (Wang et al., 2025a)	8.8415	22.4545	17.8000	23.1682	23.9000	21.8307	20.1591	**22.7773**	21.2500	**22.6455**	21.7080	23.0595	16.2381	21.9520	20.8400	20.5224
	PBE (Yang et al., 2023)	8.3789	22.4292	17.5205	22.2773	23.2273	21.3636	18.2318	21.8182	19.5955	21.2091	20.2137	24.1481	17.8025	21.5786	21.9500	21.3698
	TIGIC (Li et al., 2024b)	5.2676	17.3136	14.8045	19.0318	20.3636	17.8784	13.7045	19.4636	17.0864	18.1455	17.1000	17.7294	17.0000	21.0897	20.8828	19.1755
	TALE (Pham et al., 2024)	6.3773	19.6027	15.9863	20.4455	21.4773	19.3780	14.8318	21.6182	17.3227	18.5409	18.0784	21.6071	17.6548	21.0667	20.6933	20.2555
	TF-ICON (Lu et al., 2023d)	7.2643	20.4490	16.7538	20.8273	21.7227	19.9382	15.9045	20.1727	17.9909	19.0182	18.2716	20.9870	16.9870	21.2946	20.7984	20.0168
	DreamEdit (Li et al., 2023b)	6.0250	19.9227	16.5409	19.2773	20.5227	19.0659	14.9273	19.1818	13.3909	15.5545	15.7636	20.4714	16.8143	20.3333	20.7153	19.5836
	EEdit (Yan et al., 2025)	6.6689	18.3790	15.3379	22.0636	23.4818	19.8156	14.2091	22.2864	19.9500	21.7955	19.5603	21.1463	18.2561	22.0635	21.2222	20.6720
	Ours-Adapter	**8.8861**	23.3727	17.0500	23.5727	23.8136	21.9523	**21.3364**	22.7591	**21.3636**	22.6136	**22.0182**	23.2222	**18.7407**	**22.8448**	**22.0086**	**21.7041**
	Ours-LoRA	8.8688	**23.4545**	16.8136	**23.7727**	23.8500	**21.9727**	21.1273	22.7455	21.3000	22.5955	21.9421	**23.7590**	18.5904	22.4853	20.6765	21.3778
Complex-Compo (300)	MADD (He et al., 2024)	5.9673	13.8900	11.8167	18.8633	17.1333	15.4258	12.6800	16.7300	12.5167	10.3000	13.0567	17.6538	15.7115	20.2867	19.5533	17.2524
	ObjectStitch (Song et al., 2023)	8.8389	20.7157	13.1773	21.4200	19.4800	18.6983	17.3567	21.8500	17.1333	18.9733	18.8283	19.8304	14.6518	21.3467	19.5400	18.8394
	DreamCom (Lu et al., 2023c)	7.9884	8.2234	9.0756	**23.9178**	**23.4737**	16.1726	5.9507	**23.7072**	**22.3618**	**22.4375**	18.6143	17.8810	15.2857	22.5000	**20.9737**	19.0509
	AnyDoor (Chen et al., 2024c)	8.9760	21.7633	13.1133	20.5567	18.5300	18.4908	18.4967	21.8300	14.9267	18.1667	18.3550	22.6606	17.6422	21.2467	19.5333	19.8876
	UniCombine (Wang et al., 2025a)	8.8999	15.6747	11.2226	23.0878	22.7230	18.1770	13.7399	23.4966	20.7195	21.4554	19.8529	20.3646	15.7500	21.9764	20.2804	19.6449
	PBE (Yang et al., 2023)	8.5923	19.6151	13.1283	21.9243	20.1349	18.7007	16.8947	21.9605	17.3257	19.6217	18.9507	23.5810	14.7048	21.2039	19.6447	19.6170
	TIGIC (Li et al., 2024b)	7.6630	14.6250	11.9899	21.2357	20.0202	16.9677	12.6027	19.5185	16.9192	16.6801	16.4301	16.7168	16.5398	21.5051	20.2862	18.2956
	TALE (Pham et al., 2024)	8.7351	16.9899	11.3826	22.7600	20.7000	17.9581	15.0100	22.3567	19.0333	18.6267	18.7567	17.8317	15.4455	21.9667	19.9767	18.7955
	TF-ICON (Lu et al., 2023d)	9.3258	17.7047	12.6812	21.9463	20.4799	18.2030	15.1477	21.2919	18.1577	18.3490	18.2366	19.9775	16.7072	21.5101	19.7584	19.2380
	DreamEdit (Li et al., 2023b)	8.0434	17.2600	12.0233	18.5669	17.2578	16.2770	14.7300	19.4600	13.7467	15.6367	15.8934	23.3964	15.6396	20.4333	19.5400	18.9805
	EEdit (Yan et al., 2025)	8.7835	14.9500	11.2567	22.8746	21.8152	17.7241	13.4224	23.1485	20.2601	22.1081	19.7348	22.8058	15.6990	22.3498	20.5941	20.2367
	Ours-Adapter	9.6485	22.6162	**14.2525**	22.5552	21.9064	**20.3326**	20.4582	22.6421	18.5518	21.2876	20.7349	24.0300	17.4600	22.2074	20.3913	20.9647
	Ours-LoRA	**9.8418**	**22.9532**	13.3779	22.9130	21.7525	20.2492	**20.8328**	22.8261	19.1940	21.2776	**21.0326**	**24.3400**	**17.8900**	**22.3838**	19.9596	**21.1212**

EEdit also proposes an elegant strategy, termed inversion skipping, to accelerate the initialization process. In EEdit, the initial latent is obtained via an inversion procedure involving model predictions, while inversion skipping significantly reduces the number of required steps. In contrast, our one-step forward diffusion does not perform inversion at all. The initial latent is produced by directly sampling noise and adding it to the clean latent at a chosen timestep, without any model prediction. This makes our initialization computationally lighter. Because FLUX-Dev is a CFG-distilled model, its inversions are relatively imprecise, which we believe contributes to the weaker subject-identity preservation observed in EEdit. Our method is therefore designed to avoid reliance on accurate inversion in such distilled settings.

L Additional Image Quality Evaluation Using UnifiedReward and HPSv3

To provide a more comprehensive assessment of composition quality, we further evaluate the methods using three variants of UnifiedReward (Wang et al., 2025b;c) (UnifiedReward-2.0-qwen3vl-8b, UnifiedReward-Edit-qwen3vl-8b, and UnifiedReward-Think-qwen-7b), as well as HPSv3 (Ma et al., 2025b). The results are summarized in Tab. 6.

M Further Analysis on DSG in SD3.5

We conduct experiments on SD3.5 by replacing our DSG mechanism with standard negative prompting. Specifically, in Eqn. 3, we substitute the negative velocity $\boldsymbol{v}^{\text{neg}}_{\boldsymbol{\theta}+\Delta\boldsymbol{\theta}}$ with the velocity obtained using a variety of commonly used negative prompts. The four sets of negative prompts used are:

1. distorted, deformed, glitch, artifacts
2. undefined shapes, bad anatomy, unnatural pose
3. low quality, worst quality, low resolution, blurry, out of focus
4. AI artifacts, melted objects, strange textures

The quantitative results on the DreamEditBench dataset are presented in Tab. 7.

Key Insights These results lead to the following key conclusions:

1. **Performance Sensitivity:** The performance of standard negative prompting is sensitive to the specific wording used (e.g., Prompt 2 performs better than Prompt 4). This confirms that the effectiveness of heuristic negative prompts relies heavily on manual, often tedious, prompt engineering.

Table 7: Comparison of negative prompting versus DSG on SD3.5 on the DreamEditBench.

Method	CLIP ↑	DINO ↑	IRF ↑	DreamSim ↓	LPIPS ↓	SSIM ↑	IR ↓	VR ↑
Ours-SD3.5-Adapter (w/ NP 1)	0.7934	0.7311	0.7608	0.3918	0.0331	0.8812	0.5837	3.5714
Ours-SD3.5-Adapter (w/ NP 2)	0.8029	0.7388	0.7679	0.3781	0.0259	0.8908	0.5726	3.6102
Ours-SD3.5-Adapter (w/ NP 3)	0.7958	0.7329	0.7623	0.3892	0.0315	0.8839	0.5814	3.5796
Ours-SD3.5-Adapter (w/ NP 4)	0.7887	0.7281	0.7574	0.3976	0.0368	0.8765	0.5882	3.5548
Ours-SD3.5-Adapter (w/ DSG)	**0.8054**	**0.7407**	**0.7699**	**0.3745**	**0.0234**	**0.8937**	**0.5701**	**3.6187**

2. **Adaptive Guidance:** Standard negative prompts generate a degradation direction that is decoupled from the specifics of the input image. In contrast, DSG constructs an image-specific low-quality direction by blurring the attention component, making it significantly more adaptive, stable, and effective across diverse inputs without requiring any manual prompt tuning. DSG consistently outperforms all tested standard negative prompts across all metrics.

This analysis confirms that DSG provides a superior, more robust, and automated mechanism for degradation suppression compared to traditional negative prompting, even in models like SD3.5 where negative prompts are generally effective.

N Runtime Comparison

The wall-clock runtime at a 512×512 resolution on an H100 GPU is summarized in the table below. In our implementation, we applied qint8 quantization to all FLUX-based methods to accelerate inference and reduce GPU memory usage. Additionally, Ours-Adapter can also be run on a 24-GB GPU by enabling CPU offloading.

Table 8: Runtime and memory usage comparison of various image composition methods at a 512×512 resolution.

Method	Training Free	Base Model	External Model	Time (s)	Peak Memory (MB)
MADD (He et al., 2024)	✘	SD	DINO	45.73	11708
ObjectStitch (Song et al., 2023)	✘	SD	VIT	6.63	8268
DreamCom (Lu et al., 2023c)	✘	SD	LoRA	9.87	3388
AnyDoor (Chen et al., 2024c)	✘	SD	DINO	8.61	18612
UniCombine (Wang et al., 2025a)	✘	FLUX	LoRA	11.98	22711
PBE (Yang et al., 2023)	✘	SD	-	3.52	10842
TIGIC (Li et al., 2024b)	✔	SD	-	10.82	21640
TALE (Pham et al., 2024)	✔	SD	-	8.03	23524
TF-ICON (Lu et al., 2023d)	✔	SD	-	24.55	20670
DreamEdit (Li et al., 2023b)	✔	SD	LoRA, VIT	99.83	19298
EEdit (Yan et al., 2025)	✔	FLUX	-	60.31	26546
Ours-Adapter	✔	FLUX	Adapter	38.29	32552
Ours-LoRA	✔	FLUX	LoRA	18.08	23519

O Additional Qualitative Results

We offer more qualitative assessment results, including visualizations of all baselines, presented in Figs. 13 to 18.

P LLM Usage Statement

We used large language models for text polishing and grammar correction during manuscript preparation. No LLMs were involved in the design of the method, experiments, or analysis. All content has been carefully verified and validated by the authors.

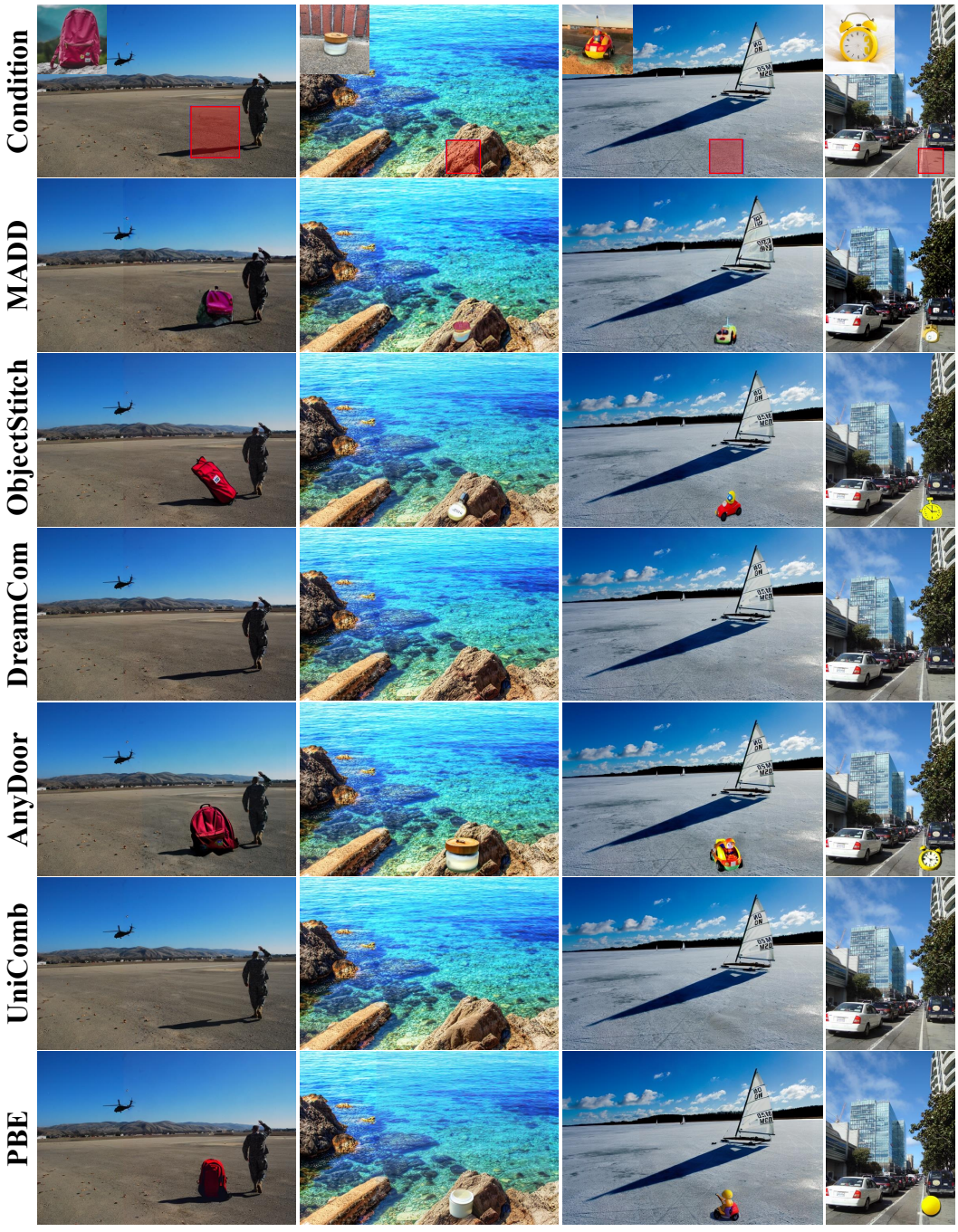

Figure 13: **(Part 1 of 2)** Qualitative comparison of our method against baselines in challenging scenarios.

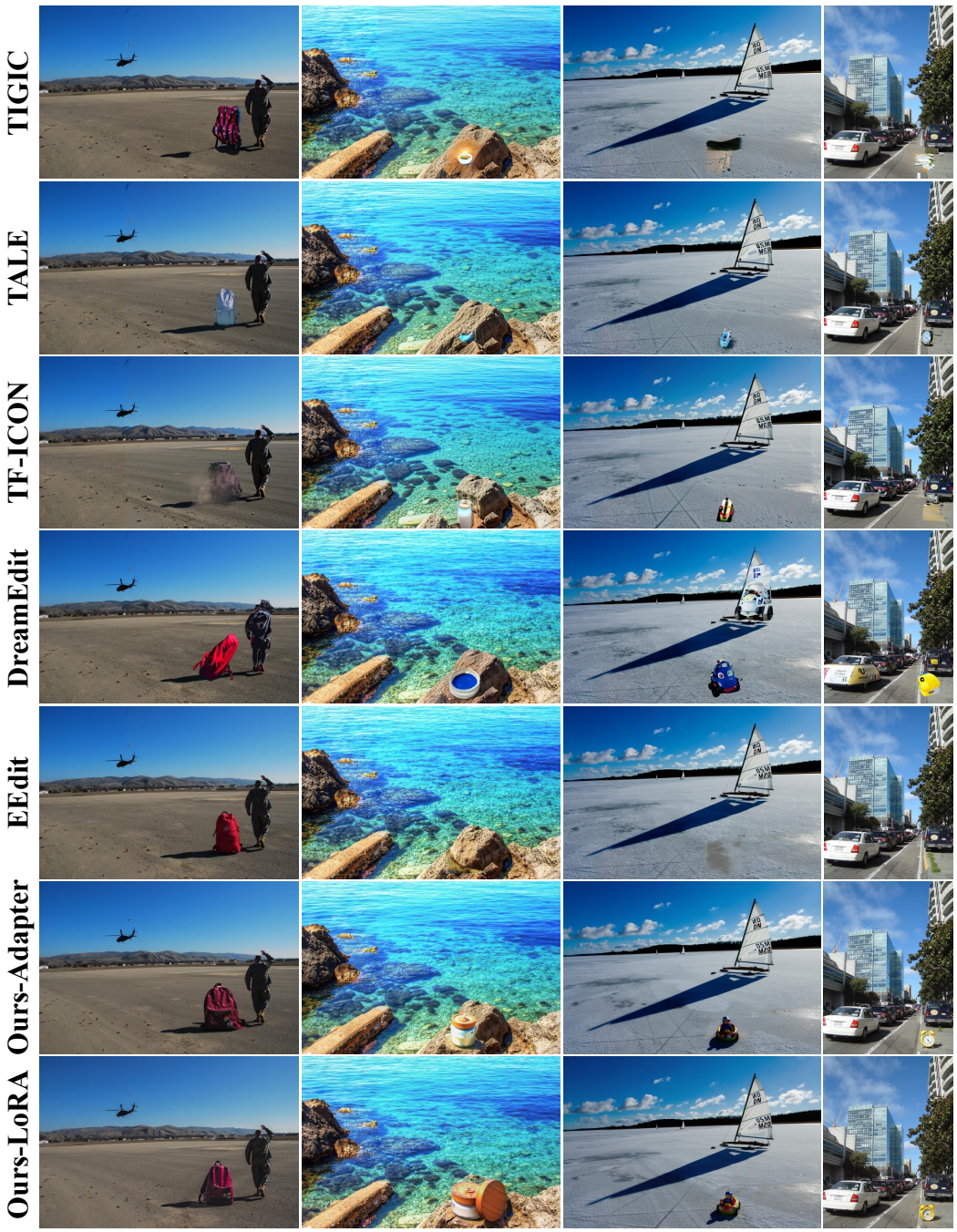

Figure 14: **(Part 2 of 2)** Qualitative comparison of our method against baselines in challenging scenarios.

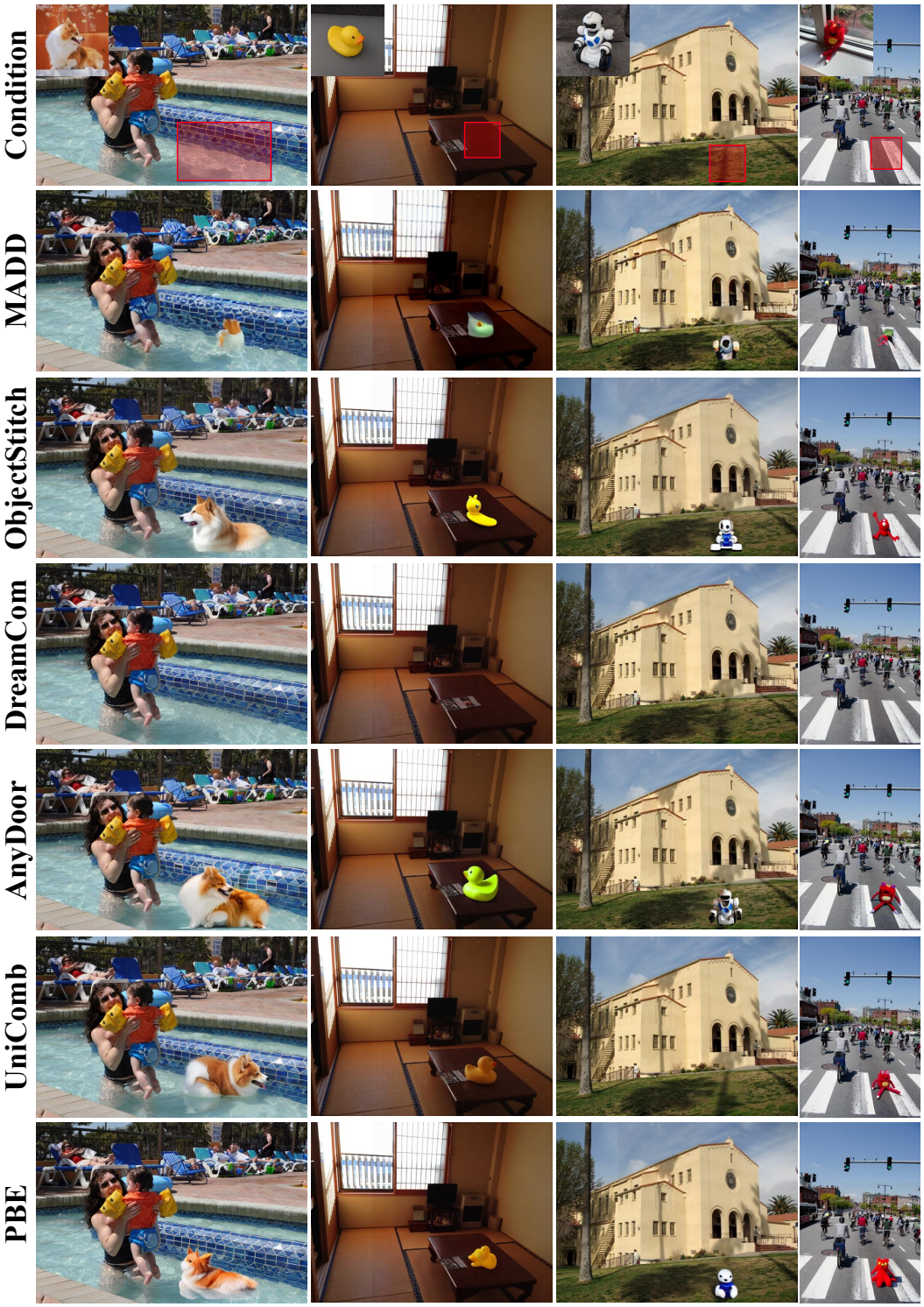

Figure 15: **(Part 1 of 2)** Qualitative comparison of our method against baselines in challenging scenarios.

Figure 16: **(Part 2 of 2)** Qualitative comparison of our method against baselines in challenging scenarios.

Figure 17: **(Part 1 of 2)** Qualitative comparison of our method against baselines in challenging scenarios.

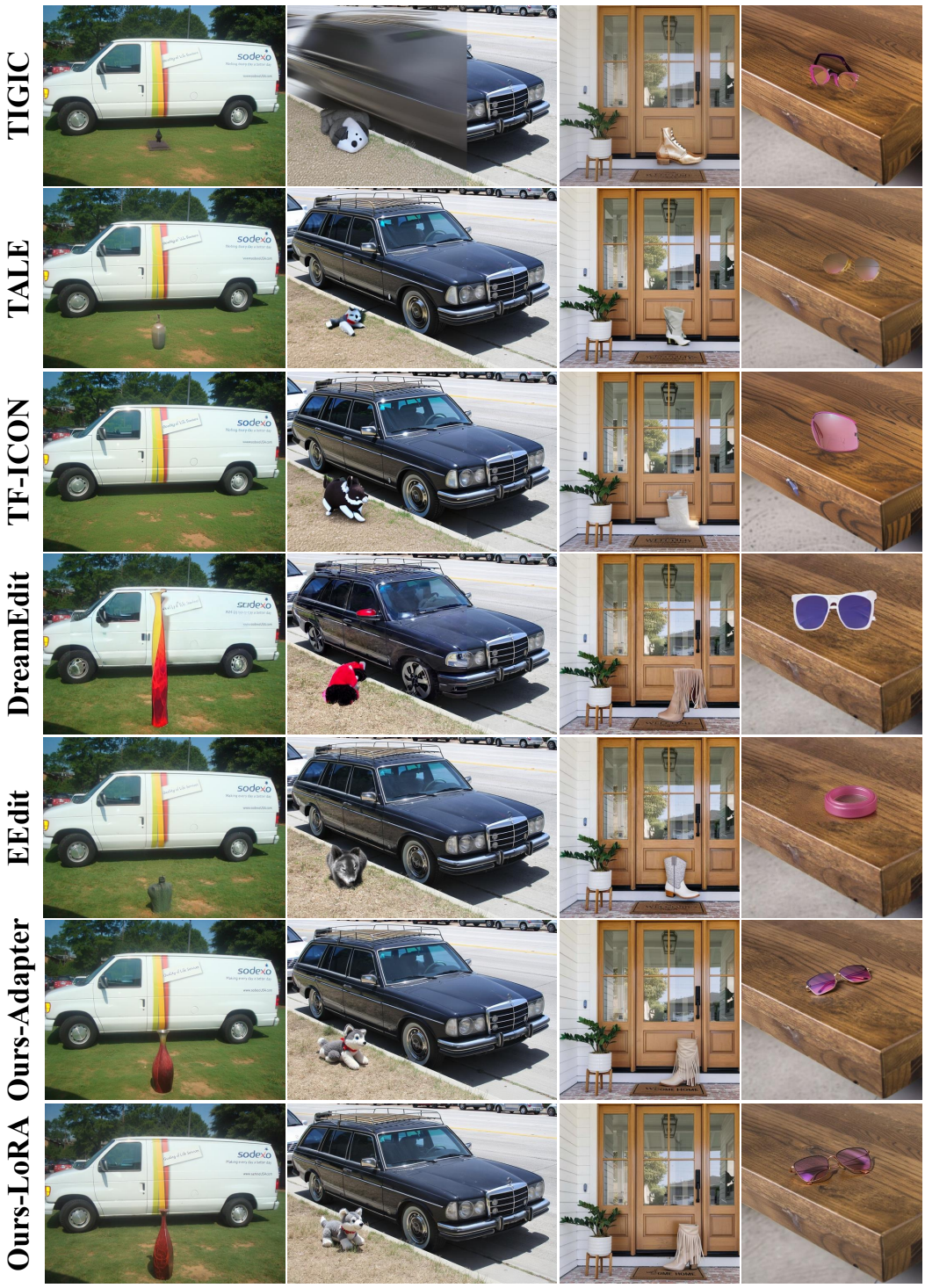

Figure 18: **(Part 2 of 2)** Qualitative comparison of our method against baselines in challenging scenarios.